Astrocytic LRRK2 Controls Synaptic Connectivity via Regulation of ERM Phosphorylation

Shiyi Wang[1,9], Ryan Baumert[1,9], Gabrielle Séjourné[1,9], Dhanesh Sivadasan Bindu[1,2], Kylie Dimond[3], Kristina Sakers[1,13], Leslie Vazquez[1,4,9], Jessica L. Moore[1,13], Christabel Xin Tan[5], Tetsuya Takano[6,7], Maria Pia Rodriguez[1], Nick Brose[1], Luke Bradley[1], Reed Lessing[1], Scott H. Soderling[1,8,9], Albert R. La Spada[10,11,12], and Cagla Eroglu[1,8,9,13]

[1]The Department of Cell Biology, Duke University Medical Center, Durham, NC, USA

[2]Department of Neonatology, Children's Mercy Hospital, Kansas City, MO, USA

[3]College of Psychology, Nova Southeastern University, Fort Lauderdale, FL, USA

[4]The Department of Neurobiology, Duke University Medical Center, Durham, NC, USA

[5]Life Sciences Institute, University of Michigan, Ann Arbor, MI, USA

[6]Division of Molecular Systems for Brain Function, Kyushu University Institute for Advanced Study, Medical Institute of Bioregulation, Japan

[7]Japan Science and Technology Agency, PRESTO, Japan

[8]The Department of Neurobiology, Duke University Medical Center, Durham, NC, USA

[9]Aligning Science Across Parkinson's (ASAP) Collaborative Research Network, Chevy Chase, MD

[10]The Department of Neurology, Duke University Medical Center, Durham, NC, USA

[11]Departments of Pathology & Laboratory Medicine, Neurology, Biological Chemistry, and Neurobiology & Behavior, University of California, Irvine, CA, USA

[12]UCI Center for Neurotherapeutics, University of California, Irvine, CA, USA

[13]Howard Hughes Medical Institute, Duke University Medical Center, Durham, NC, USA

Corresponding authors: Shiyi Wang: shiyi.wang@duke.edu;

Albert R. La Spada: alaspada@uci.edu;

Cagla Eroglu: cagla.eroglu@duke.edu

Abstract

Astrocytes regulate synaptic connectivity. However, whether astrocyte dysfunction causes synaptic pathologies in disorders such as Parkinson's Disease (PD) is unknown. Here, we investigated how the most common Parkinsonism gene mutation, *LRRK2* G2019S, impacts structure and synaptogenic function of cortical astrocytes. In human and mouse cortex, the LRRK2 G2019S mutation caused astrocyte morphology deficits and enhanced the phosphorylation of the ERM proteins (Ezrin, Radixin, and Moesin), components of the perisynaptic astrocyte processes. Reducing ERM phosphorylation in LRRK2 G2019S mouse astrocytes restored astrocyte morphology and corrected excitatory synaptic deficits. Using an *in vivo* BioID proteomic approach, we found astrocytic Ezrin interacts with Atg7, a master regulator of autophagy. The Ezrin/Atg7 interaction is inhibited by Ezrin phosphorylation and thus diminished in LRRK2 G2019S astrocytes. Importantly, Atg7 function is required to maintain proper astrocyte morphology. These studies reveal an astrocytic molecular mechanism that could serve as a therapeutic target for synaptic pathologies seen in PD.

INTRODUCTION

Most synapses in the central nervous system are in direct contact with perisynaptic astrocyte processes (PAPs)[1], forming the "tripartite synapse"[1]. At the tripartite synapse, astrocytes clear excess neurotransmitters, maintain ion homeostasis, and secrete factors regulating synapse development and function[2]. To accomplish these crucial functions, astrocytes develop elaborate morphologies and form a gap junction-coupled network that tiles the entire brain parenchyma[3-5]. Astrocyte morphogenesis, tiling, and synaptogenesis are interdependent and bidirectional[6,7]. In neurological disorders like PD, astrocytes become reactive, undergoing morphological and molecular changes[8,9].

Mutations in the leucine-rich repeat kinase 2 (*LRRK2*) gene cause familial PD[10,11], with LRRK2 G2019S being the most common[12-14]. It is largely accepted that LRRK2 G2019S is a gain-of-function mutation that increases LRRK2's kinase activity[15-20]. PD patients with the LRRK2 G2019S mutation exhibit symptoms resembling idiopathic PD, including late onset, L-DOPA responsiveness, and Lewy body pathology[21,22]. These patients also experience non-motor symptoms like depression, hallucinations, and cognitive deficits[13,14,23]. While rodent models with the LRRK2 G2019S mutation lack motor dysfunction or dopaminergic neuron loss[24-26], they exhibit cognitive impairments linked to cortical and cortico-striatal dysfunction[27,28], reflecting critical non-motor symptoms of PD[29-38].

It is widely accepted that neuronal dysfunction drives synaptic pathologies in PD; however, given the important roles of astrocytes in synaptic connectivity, astrocyte dysfunction may underlie the circuit phenotypes. ERM proteins (Ezrin, Radixin, and Moesin) are structural components of perisynaptic astrocyte processes[39,40]. When

67 phosphorylated and bound to phosphatidylinositol 4,5-bisphosphate (PIP2), ERM
68 proteins change conformation and link F-actin and other proteins to the cell
69 membrane[41,42]. Previous studies suggested ERM proteins as potential substrates of the
70 kinase activity of LRRK2[17,43,44]. Therefore, we tested whether LRRK2 may mediate
71 astrocyte function through the regulation of ERM phosphorylation using the LRRK2
72 G2019S knockin ($^{ki/ki}$) mouse model[33,45] in conjunction with *in vivo* astrocyte-specific
73 genetic, proteomic, electrophysiological, and biochemical approaches. We revealed that
74 the Lrrk2 G2019S genotype enhances ERM phosphorylation in cortical astrocytes, which
75 impacts astrocyte morphology and synaptic connectivity. Dampening ERM
76 phosphorylation levels in LRRK2 G2019S mouse astrocytes can rescue astrocyte
77 morphology and excitatory synaptic deficits in the anterior cingulate cortex (ACC),
78 suggesting a mechanism through which the LRRK2 G2019S mutation disrupts astrocyte
79 morphology and synaptic connectivity.

80 **RESULTS**

81 **LRRK2 G2019S mutation causes ERM hyperphosphorylation in the prefrontal**
82 **cortices of mice and humans.**

83 To study how the LRRK2 G2019S mutation impacts astrocytes in the prefrontal
84 cortex, a cortical region linked to PD, we stained sections from the frontal cortices of age-
85 and sex-matched control and LRRK2 G2019S mutation-carrying PD patients
86 (Supplemental Table 1) with glial fibrillary acidic protein (GFAP, a marker for astrocyte
87 branches) and phosphorylated ERM (Phospho-ERM, which are enriched in PAPs) (Figure
88 1A). Remarkably, the astrocytic organization, determined by GFAP staining, was severely

89 disrupted, and GFAP levels were significantly elevated (~42%) in PD patients carrying
90 the LRRK2 G2019S mutation, indicative of reactive gliosis (Figure 1B-C). Unexpectedly,
91 the phospho-ERM signal was increased by 7-fold in the frontal cortices of PD patients
92 carrying the LRRK2 G2019S mutation (Figure 1B-C). The elevated phospho-ERM signal
93 was observed in GFAP-positive astrocytes and other cortical cells. These data reveal that
94 there are reactive astrocytes in the cortices of LRRK2 G2019S PD patients, and ERM
95 phosphorylation is highly upregulated in the brains of these patients.

96 To determine whether ERM hyperphosphorylation is an early or late event in
97 LRRK2 G2019S PD pathology, we used LRRK2 G2019S$^{ki/ki}$ mice, in which the human
98 G2019S mutation was introduced into exon 41 of the Lrrk2 gene[33,45]. To determine if ERM
99 hyperphosphorylation localizes to astrocytes, we crossed these mice to an astrocyte
100 reporter line carrying the Aldh1L1-eGFP transgene, which labels all astrocytes by GFP[46].
101 We examined the phospho-ERM levels in coronal brain sections from 21-day-old (P21,
102 juvenile) and 12-week-old (P84, adult) wild-type (WT) or LRRK2 G2019S$^{ki/ki}$ mice. In
103 LRRK2 G2019S$^{ki/ki}$ mice, a brain region-specific and heterogeneous increase in phospho-
104 ERM staining was observed in astrocytes across both age groups compared to WT mice
105 (Figure 1D-L). The increase in phospho-ERM in LRRK2 G2019S$^{ki/ki}$ mice was localized to
106 layers (L)1 and L2-3 of the anterior cingulate cortex (ACC) and the primary motor cortex
107 (MOp) (Figure 1E-L; Figure S1A-C) but was absent in other regions such as the primary
108 sensory cortex (SSp) and the dorsal medial striatum (DMS) (Figure S1D-I). In P21 LRRK2
109 G2019S$^{ki/ki}$ mice, the phospho-ERM integrated densities in the ACC and MOp L1 and L2-
110 3 were increased by ~32% (ACC) and ~41% (MOp) compared to the WTs (Figure 1I),

111 whereas in P84 LRRK2 G2019S$^{ki/ki}$ mice, the phospho-ERM integrated densities were
112 increased by ~57% (ACC) and ~37% (MOp) compared to the WTs (Figure 1L).

113 To confirm the specificity of the phospho-ERM antibody, we treated brain sections
114 from both mouse and human samples with lambda protein phosphatase (λ-PPase). The
115 phospho-ERM signal was eliminated after λ-PPase treatment in both human and mouse
116 tissues, confirming the phospho-ERM antibodies' specificity (Figure S2A-F). We then
117 investigated if the ERM hyperphosphorylation was cell type-specific by co-staining
118 phospho-ERM with various cellular markers. In the ACC and MOp L1 and L2/3 of LRRK2
119 G2019S$^{ki/ki}$ mice, phospho-ERM was significantly increased and colocalized with S100β
120 (astrocyte marker) and MAP2 (neuronal marker) but not Iba1 (microglia marker), with a
121 predominant localization to astrocytes in the ACC and MOp of LRRK2 G2019S$^{ki/ki}$ mice
122 (Figure S3A-C). In the frontal cortices of PD patients carrying the LRRK2 G2019S
123 mutation, we found significant increases in phospho-ERM signal colocalized with S100β
124 and MAP2 (Figure S3D-F), indicating ERM hyperphosphorylation is significantly elevated
125 in astrocytes and neurons in both mice and human carrying the LRRK2 G2019S mutation.
126 Importantly, we did not observe any difference in total ERM levels in the ACC and MOp
127 between WT and LRRK2 G2019S$^{ki/ki}$ brain sections (Figure S4A-C), suggesting the
128 observed ERM hyperphosphorylation was due to the phosphorylation status of ERM
129 rather than ERM protein expression.

130 These findings reveal that the LRRK2 G2019S mutation increases phospho-ERM
131 levels in the cortices of PD patients and mice. In the human samples, phospho-ERM
132 elevation was observed concurrently with reactive gliosis (elevated GFAP staining). To
133 determine if, in LRRK2 G2019S$^{ki/ki}$ mice, there were reactive astrocytes detectable at

134 early ages, we stained sections from the same P21 mouse brains with an anti-GFAP
135 antibody. In the mouse cortex, grey matter astrocytes do not display GFAP staining
136 unless there is reactive gliosis[47,48]. We did not detect any increase in the levels of GFAP
137 (Figure S4D-F), indicating that phospho-ERM upregulation does not occur concurrently
138 with reactive astrogliosis in LRRK2 G2019S$^{ki/ki}$ mice. Distinct from the P21 and P84
139 LRRK2 G2019S$^{ki/ki}$ mice where phospho-ERM was restricted to a subset of astrocytes in
140 a brain region-specific manner, in the human patient brains (~80 years old), phospho-
141 ERM accumulation was present equally in both astrocytes and neurons. These data
142 suggest that ERM hyperphosphorylation is an early and astrocyte-specific event in
143 LRRK2 G2019S$^{ki/ki}$ mice but becomes more widespread and affects neurons in late-stage
144 PD in humans.

145 **LRRK2 G2019S mutation alters excitatory and inhibitory synapse numbers and**
146 **function in the cortex.**

147 Previous studies did not observe dopaminergic neuron loss or motor dysfunction
148 in the LRRK2 G2019S$^{ki/ki}$ mice[25,26]; however, synapse dysfunction at cortico-striatal
149 circuits was reported in adult mice[35]. Despite the critical role of Lrrk2 in cortico-striatal
150 synapses and PD-related cortical circuits[49], whether LRRK2 G2019S affects cortical
151 synapse numbers and function has not been explored. Understanding these cortical
152 synaptic abnormalities is crucial, as they may underlie the early cognitive deficits in PD
153 that are unrelated to dopaminergic dysfunction. Therefore, we investigated how LRRK2
154 G2019S mutation impacts synaptic connectivity in the ACC and MOp L1 and L2-3 (Figure
155 2A), regions in which ERM hyperphosphorylation within astrocytes was observed.

156 We quantified the density of excitatory and inhibitory intracortical synapses in WT
157 and LRRK2 G2019S$^{ki/ki}$ mice. To do so, we marked the excitatory synapses as the co-
158 localization of the presynaptic Vesicular Glutamate Transporter 1 (VGlut1) and the
159 Postsynaptic Density Protein (PSD95), whereas inhibitory synapses were labeled using
160 presynaptic Vesicular GABA Transporter (VGAT) and postsynaptic gephyrin
161 (GEPHYRIN)[50,51] (Figure 2B). Structural synapses were identified as the apposition and
162 co-localization of presynaptic and postsynaptic markers, which are in two distinct
163 neuronal compartments (i.e., axons and dendrites) and would only appear to co-localize
164 at synapses due to their proximity[52].

165 Excitatory synapse densities were quantified both at P21 and P84. In the ACC of
166 the LRRK2 G2019S$^{ki/ki}$ mice, there was a significant decrease in intracortical excitatory
167 synapse densities in both layers and ages we analyzed (~30%) when compared to the
168 WT controls (Figure 2C-D and Figure S5A-B). However, no differences in excitatory
169 synapse numbers were observed between genotypes in the MOp (Figure 2E-F and Figure
170 S5C-D). When we quantified the densities of inhibitory synapses in the MOp, we found
171 significant differences between genotypes (~40% increase). In contrast, no differences
172 were observed for inhibitory synapse numbers in the ACC of WT and LRRK2 G2019S$^{ki/ki}$
173 mice (Figure 2G-J). These results revealed that the LRRK2 G2019S mutation causes a
174 brain region-specific reduction in excitatory synapse densities in the ACC and an increase
175 in inhibitory synapse densities in the MOp, highlighting synaptic alterations associated
176 with this mutation.

177 Next, we used electrophysiology to assess how altered synapse density in the
178 ACC and MOp of LRRK2 G2019S$^{ki/ki}$ mice affects synaptic function. We recorded

179 miniature excitatory postsynaptic currents (mEPSCs) in the ACC L2-3 pyramidal neurons
180 and miniature inhibitory postsynaptic currents (mIPSCs) in the MOp L2-3 pyramidal
181 neurons from acute brain slices of P84 WT and LRRK2 G2019S$^{ki/ki}$ mice. LRRK2
182 G2019S$^{ki/ki}$ neurons displayed a ~65% reduction in mEPSC frequency and a
183 corresponding right shift in the cumulative distributions of mEPSC inter-event intervals
184 (Figure 3A-B) when compared to WT neurons, with no change in mEPSC amplitude
185 (Figure 3C). mEPSC frequency changes correlate with synapse numbers and/or the
186 probability of presynaptic glutamate release[53], whereas mEPSC amplitude indicates the
187 synaptic strength reflecting the number of AMPARs at the postsynapse[54]. Therefore,
188 together with our anatomical data, these findings suggest that the LRRK2 G2019S
189 mutation reduces the number of intracortical excitatory connections formed on L2-3
190 pyramidal neurons in the ACC without altering synaptic strength. In contrast, in the MOp,
191 LRRK2 G2019S$^{ki/ki}$ neurons exhibited a ~72% increase in mIPSC frequency compared to
192 WT, with no significant change in amplitude (Figure 3D-F). This data aligns with our
193 findings that inhibitory synapse numbers are elevated in the MOp of LRRK2 G2019S$^{ki/ki}$
194 mice.

195 **Reducing ERM hyperphosphorylation in astrocytes rescues excitatory synapse**
196 **density and function in the ACC of adult LRRK2 G2019S$^{ki/ki}$ mice.**

197 Lrrk2 phosphorylates a conserved threonine residue present in all ERM
198 proteins[17,43]. We found that LRRK2 G2019S mutation increases ERM phosphorylation in
199 astrocytes (Figure 1) and hypothesized that dampening ERM phosphorylation in
200 astrocytes could restore the synapse alteration in LRRK2 G2019S$^{ki/ki}$ mice. To test this,

201 we overexpressed a phospho-dead Ezrin mutant, which cannot be phosphorylated, in
202 astrocytes via adenovirus (AAV) retro-orbital injection. We chose Ezrin because Ezrin is
203 highly abundant and specifically enriched in astrocytes compared to its family members,
204 Radixin and Moesin[55] (Figure S6A-B). Switching the amino acid threonine (T) at location
205 567 with alanine (A) results in a version of the protein that cannot be phosphorylated
206 (Phospho-dead Ezrin, Figure S6C)[42,56].

207 To determine if phospho-dead Ezrin can reduce ERM phosphorylation in
208 astrocytes of LRRK2 G2019S$^{ki/ki}$ mice, we retro-orbitally injected 9-week-old WT and
209 LRRK2 G2019S$^{ki/ki}$ mice with AAVs to express Hemagglutinin (HA)-tagged WT Ezrin or
210 phospho-dead Ezrin under the control of the astrocyte-specific GfaABC1D promoter
211 (Figure S6D). The injected mouse brains were harvested at 12 weeks (3 weeks after
212 injection) for histological analyses. The widespread viral expression of Ezrin in astrocytes
213 was verified by staining with an anti-HA tag antibody (Figure 4A). While WT or phospho-
214 dead Ezrin overexpression had no effect on ERM phosphorylation in WT brains, WT Ezrin
215 increased phospho-ERM levels in LRRK2 G2019S$^{ki/ki}$ astrocytes, whereas phospho-dead
216 Ezrin abolished this increase (Figure 4A-B). This indicates that the LRRK2 G2019S
217 mutation sensitizes astrocytes to Lrrk2-mediated ERM phosphorylation. To determine the
218 specificity of phospho-dead Ezrin, we examined hyperphosphorylation of another Lrrk2
219 substrate, Rab10 (Thr 73)[18,20,57]. We found higher Rab10 phosphorylation in LRRK2
220 G2019S$^{ki/ki}$ brain sections than in WT mice. However, neither WT nor phospho-dead Ezrin
221 overexpression impacted Rab10 phosphorylation (Figure S7), showing that phospho-
222 dead Ezrin selectively reduces ERM hyperphosphorylation in astrocytes.

223 We next tested whether reducing ERM hyperphosphorylation in astrocytes could
224 rescue synaptic deficits in LRRK2 G2019S$^{ki/ki}$ ACC and MOp. While WT Ezrin
225 overexpression in astrocytes had no significant changes on excitatory synapse density in
226 the WT ACC (Figure S8), phospho-dead Ezrin reduced excitatory synapse density by ~30%
227 compared to WT mice overexpressing WT Ezrin (Figure 4C-D). Conversely, astrocytic
228 overexpression of phospho-dead Ezrin in LRRK2 G2019S$^{ki/ki}$ restored excitatory synapse
229 numbers to levels comparable to those in the WT ACC overexpressing WT Ezrin (Figure
230 4C-D). These findings suggest that the reduced synapse numbers in the ACC of the
231 LRRK2 G2019S$^{ki/ki}$ mice is due to astrocytic dysfunction from dysregulated ERM
232 phosphorylation. They also indicate that astrocytes play a key role in excitatory synaptic
233 dysfunction in the LRRK2 G2019S$^{ki/ki}$ mouse cortex.

234 We next investigated whether the same manipulation of adult astrocytes can
235 change the inhibitory synapse number in the MOp. We found that neither the WT nor the
236 phospho-dead Ezrin overexpression in adult astrocytes can rescue the density of
237 inhibitory synapses back to the levels in the WT MOp overexpressed with WT Ezrin in the
238 MOp L1 and L2-3 of LRRK2 G2019S$^{ki/ki}$ mice (Figure S9). In summary, phospho-dead
239 Ezrin expression in adult WT or LRRK2 G2019S$^{ki/ki}$ astrocytes is sufficient to modify
240 excitatory synapse numbers in the ACC but cannot restore or impair inhibitory synaptic
241 connectivity in the MOp. It is plausible that LRRK2 G2019S mutation impairs inhibitory
242 synapses in the MOp by altering the number or connectivity of cortical interneurons
243 through a developmental mechanism. Thus, manipulation in adults is insufficient to
244 eliminate this inhibitory synapse phenotype.

245 Because astrocytic overexpression of phospho-dead Ezrin impacted excitatory
246 synapse numbers in the ACC of WT and LRRK2 G2019S$^{ki/ki}$ mice, we next performed
247 whole-cell patch-clamp recordings from ACC L2-3 pyramidal neurons transduced with the
248 same AAVs. Overexpression of WT Ezrin in LRRK2 G2019S$^{ki/ki}$ astrocytes did not rescue
249 the decreased frequency of mEPSCs in ACC L2-3 neurons. However, overexpression of
250 phospho-dead Ezrin in LRRK2 G2019S$^{ki/ki}$ astrocytes restored the frequency up to the
251 levels of WT mice expressing WT Ezrin (Figure 4E-F). Interestingly, overexpression of
252 phospho-dead Ezrin in WT astrocytes significantly reduced the frequency of mEPSCs
253 (~54%) in WT ACC neurons (Figure 4E-F). Posthoc comparisons confirmed no significant
254 differences in mean mEPSC amplitudes across all 4 conditions (Figure 4G).

255 Altogether, these electrophysiological and neuroanatomical analyses show that
256 the LRRK2 G2019S mutation reduces the density and function of excitatory synaptic
257 inputs made onto the ACC L2-3 but increases the density and function of inhibitory
258 synaptic inputs made onto the MOp L2-3. These data reveal that the LRRK2 G2019S
259 mutation dysregulates proper excitatory and inhibitory synapse connectivity and function
260 in the cortex in a brain region-specific manner. These results also pinpoint a link between
261 LRRK2 G2019S-mediated ERM hyperphosphorylation in astrocytes (Figure 1) and the
262 excitatory synaptic dysfunctions in the ACC (Figure 2 and 3). Our results show that
263 astrocytic overexpression of phospho-dead Ezrin in adult LRRK2 G2019S$^{ki/ki}$ mice can
264 recover excitatory synapse density and function, whereas the same manipulation disrupts
265 synapse numbers and function in WT ACC neurons (Figure 4). These findings show that
266 balancing ERM phosphorylation in astrocytes is crucial for maintaining excitatory synapse
267 density and function in the ACC.

268 **Lrrk2 regulates astrocyte morphological complexity *in vivo* through ERM**
269 **phosphorylation.**

270 Astrocytes are critical for synaptic function and brain development, and their
271 morphology at P21 can have significant implications for synaptic connectivity and network
272 activity in adulthood[5]. Based on our observation that ERM hyperphosphorylation in
273 LRRK2 G2019S$^{ki/ki}$ astrocytes disrupts cortical synaptic connectivity at P21, we next
274 investigated how this mutation impacts astrocyte morphological complexity.

275 To determine if astrocyte morphology was altered in the LRRK2 G2019S$^{ki/ki}$
276 cortices, we sparsely labeled astrocytes with a membrane-targeted fluorescent protein
277 (mCherry-CAAX) using postnatal astrocyte labeling by electroporation (PALE) in WT and
278 LRRK2 G2019S$^{ki/ki}$ mice and imaged whole astrocytes with confocal microscopy at high
279 resolution (Figure S10A). We focused our analyses of astrocyte territory size and
280 complexity (see Methods for details) on the ACC and MOp L1 and L2-3 at P21. In LRRK2
281 G2019S$^{ki/ki}$ mice, the territory volumes of astrocytes were significantly smaller (reduced
282 by ~34%) than WT astrocytes (Figure 5A-B), without altering the number of
283 ALDH1L1+/SOX9+ cells in the ACC and MOp (Figure S10B-D). These results reveal that
284 LRRK2 G2019S mutation reduces astrocyte morphological complexity without affecting
285 astrocyte numbers *in vivo*.

286 Because phospho-dead Ezrin overexpression in astrocytes differentially impacts
287 synapse numbers and function in WT and LRRK2 G2019S$^{ki/ki}$ mice (Figure 4), we
288 hypothesized that overexpression of phospho-dead Ezrin would also impact astrocyte
289 morphology differently between genotypes. We found that the overexpression of

290 phospho-dead Ezrin decreased the territory volume and morphological complexity of WT
291 astrocytes but restored astrocyte territory volume and complexity in LRRK2 G2019S$^{ki/ki}$
292 mice (Figure 5A-C). Our results show that the abundance of unphosphorylated Ezrin
293 differentially regulates astrocyte morphology in WT versus LRRK2 G2019S$^{ki/ki}$ astrocytes.

294 Previous studies suggested phosphorylation at T567 promotes Ezrin acquiring an
295 open conformation by binding to phosphatidylinositol-4,5-bisphosphate (PIP2)[58]. In this
296 conformation, the N-terminus interacts with membrane proteins, and the C-terminus is
297 available to bind to the actin cytoskeleton[59,60]. An Ezrin mutant in which the T567 residue
298 is switched with aspartate (D) prefers Ezrin's open conformation, thereby mimicking the
299 phosphorylated state (Phospho-mimetic Ezrin, Figure S4C)[61,62]. Conversely, the
300 phospho-dead Ezrin remains in the closed conformation in which the N and C terminal
301 domains are bound together. This closed conformation is proposed to be unable to
302 interact with membranes or actin[56,63]. Because we found that phospho-dead Ezrin
303 differentially impacts WT and LRRK2 G2019S$^{ki/ki}$ astrocytes, we hypothesized that Ezrin's
304 transition between open and closed conformation is regulated by LRRK2 function and
305 should be tightly balanced for proper astrocyte morphogenesis (Figure 5D). In LRRK2
306 G2019S$^{ki/ki}$ astrocytes, Ezrin is more likely to be phosphorylated and in the open state.
307 This distorted balance of the Ezrin state may explain the morphological defects of LRRK2
308 G2019S$^{ki/ki}$ astrocytes. This model also aligns with our findings that dampening Ezrin
309 phosphorylation via phospho-dead Ezrin disrupts WT astrocyte morphology but rescues
310 the deficits in LRRK2 G2019S$^{ki/ki}$ astrocytes.

311 If this model is correct, we would expect that the loss of Lrrk2 function in astrocytes
312 impacts astrocyte morphogenesis, a phenotype that we could rescue by introducing

313 phospho-mimetic Ezrin. To test the impact of Lrrk2 loss in astrocytes, first, we used a
314 knockout (KO)-verified Lrrk2 antibody[64,65] and confirmed the expression of Lrrk2 protein
315 in cortical mouse astrocytes by immunostaining coronal brain sections from WT or LRRK2
316 G2019S$^{ki/ki}$ mice. Lrrk2 staining was evident in WT and LRRK2 G2019S$^{ki/ki}$ astrocytes,
317 localizing throughout astrocytic processes (Figure S11A-B). In addition, cortical
318 astrocytes isolated from WT rats express Lrrk2 *in vitro,* which was detected by
319 immunoblotting (Figure S11C-D). In agreement, RNA sequencing databases for cortical
320 cell types in mice and humans also show LRRK2 mRNA present in astrocytes (Fig. S11C-
321 D). To test if astrocytic Lrrk2 function is required to control astrocyte morphogenesis, we
322 knocked down Lrrk2 in WT astrocytes *in vivo*, using PALE. Astrocytes transfected with
323 shLrrk2 (~90% Lrrk2 reduction, Figure S11E-F) exhibited significantly smaller territory
324 volumes (~36% reduction) and reduced complexity, similar to LRRK2 G2019S$^{ki/ki}$
325 astrocytes (Figure 5E-G). Overexpression of phospho-mimetic Ezrin restored shLrrk2-
326 containing astrocyte territory volume and morphological complexity up to the levels of
327 shControl-transfected astrocytes (Figure 5E-G) but had no effect in shControl-transfected
328 astrocytes (Figure 5E-G).

329 These results show that both the gain of Lrrk2 kinase function (in LRRK2
330 G2019S$^{ki/ki}$ mice) and the loss of Lrrk2 function (shLrrk2) decrease astrocyte complexity
331 and size. The opposite manipulation of Ezrin conformational/phosphorylation states can
332 rescue these morphological phenotypes. These results are in line with a model that
333 indicates that both the loss and gain of LRRK2 function would cause astrocyte
334 morphology deficits by causing an imbalance between the phosphorylated and
335 unphosphorylated ERM levels, albeit in opposite directions. By overexpressing phospho-

336 mimetic Ezrin in shLRRK2 astrocytes, shLRRK2 astrocyte morphology was rescued,
337 supporting our model. In the control astrocytes, however, overexpression of phospho-
338 mimetic Ezrin did not cause a reduction in astrocyte territory and morphological
339 complexity. This outcome can be explained by the presence of endogenous
340 unphosphorylated Ezrin, which can balance the phospho-mimetic Ezrin. Together, these
341 findings indicate that LRRK2 kinase function plays a critical role in regulating astrocyte
342 morphological complexity through ERM phosphorylation homeostasis *in vivo*.

343 **LRRK2 G2019S mutation interrupts Ezrin interactomes in astrocytes.**

344 To investigate how ERM hyperphosphorylation affects astrocyte morphology in
345 LRRK2 G2019S$^{ki/ki}$ astrocytes, we identified possible Ezrin interactors in WT and LRRK2
346 G2019S$^{ki/ki}$ astrocytes using *in vivo* astrocyte-specific proximity labeling. We used two
347 virally encoded astrocyte-specific biotin ligase probes: Ezrin fused with BioID (Astro-
348 Ezrin-BioID) and soluble BioID with a nuclear export sequence (Astro-Cyto-BioID) (Figure
349 6A). These probes were delivered via intracortical AAV injections to P0-2 WT and LRRK2
350 G2019S$^{ki/ki}$ mouse pups and followed by subcutaneous biotin injections starting at P18
351 for 3 days and tissue collection at P21 (Figure 6B). Biotinylated proteins were detected in
352 astrocytes using immunohistochemistry and immunoblotting for HA and Streptavidin
353 (Figure S12).

354 Affinity-purified proteins from cortices were analyzed using quantitative liquid
355 chromatography-tandem mass spectrometry (LC-MS) (Figure 6B), identifying 30,815
356 unique peptides corresponding to 4,081 unique proteins (Supplemental Tables 2-4).
357 Principle component analyses (PCA) of BioID results showed distinct clustering between
358 Cyto-BioID (control) and Ezrin-BioID (bait) samples, with further separation between WT

359 or LRRK2 G2019S$^{ki/ki}$ astrocytes (Figure S13A). Radixin and Moesin, known Ezrin family
360 proteins, were significantly enriched in the Ezrin-BioID sample compared to Cyto-BioID
361 (Figure S13B)[66]. Comparative analysis revealed 344 proteins with significantly altered
362 proximity to Ezrin in LRRK2 G2019S$^{ki/ki}$ astrocytes (fold-change >1.5 or < -1.5, $p < 0.05$);
363 190 and 154 proteins gained and lost Ezrin proximity, respectively (Figure 6C; Figure
364 S13C-D; Supplemental Table 5). Gene Ontology (GO) analysis of these proteins showed
365 phospholipid binding, microtubule binding, and membrane transporter and cell-adhesion
366 mediator activity were over-represented in differentially enriched proteins (Figure 6D;
367 Supplemental Table 6). This result aligns with our model that the LRRK2 G2019S
368 mutation would shift Ezrin towards its phosphorylated/open state, promoting membrane
369 interactions. Unexpectedly, GO-term analyses of biological processes highlighted
370 enrichment in catabolic processes, macroautophagy, negative regulation of
371 developmental growth, and intracellular transport (Figure 6E; Supplemental Table 7).
372 These findings indicated that Ezrin plays a role in these biological processes, which are
373 altered by the LRRK2 G2019S mutation.

374 Previous studies showed macroautophagy deficits in neurons with the LRRK2
375 G2019S mutation[67]. To assess global cytosolic changes, we analyzed the Astro-Cyto-
376 BioID dataset across genotypes, identifying 195 differentially enriched proteins (78 gained,
377 117 lost in LRRK2 G2019S$^{ki/ki}$; Figure S9E; Supplemental Table 8). GO-term analysis
378 revealed an enrichment of proteins associated with phospholipid binding and vesicle
379 trafficking (Figure S13F-G; Supplemental Tables 9-10). However, macroautophagy-
380 related terms were not enriched, suggesting that the observed changes in Ezrin-BioID
381 are specifically related to alterations in Ezrin function in LRRK2 G2019S$^{ki/ki}$ astrocytes.

382 BioID captures proteins in close proximity to the bait but does not guarantee direct
383 interactions. To identify potential direct Ezrin interactors affected by LRRK2 G2019S, we
384 compared protein abundance in Astro-Ezrin-BioID to Astro-Cyto-BioID within each
385 genotype (Ezrin/Cyto fold -change > 1.5, $p > 0.05$, 346 proteins in WT and 335 proteins
386 in LRRK2 G2019S$^{ki/ki}$; Supplemental Tables 11-12). To generate high-confidence lists of
387 interactors that gained or lost proximity to Ezrin in LRRK2 G2019S$^{ki/ki}$ astrocytes, we set
388 a second requirement for proteins with fold-change > 1.5 or < -1.5 between LRRK2
389 G2019S$^{ki/ki}$ and WT Astro-Ezrin-BioID. Using these filters, we narrowed our list down to
390 28 proteins that "gained proximity to Ezrin in LRRK2 G2019S astrocytes" and 30 proteins
391 that "lost proximity to Ezrin in LRRK2 G2019S astrocytes" (Figure 6F-H; Supplemental
392 Table 13). Upregulated proteins, such as Rala, Cops3, and Anks1a, are involved in
393 vesicular trafficking, cell signaling, and cytoskeletal regulation, aligning with enhanced
394 ERM phosphorylation and their recruitment to the plasma membrane. In contrast, the
395 downregulated proteins (e.g., Atg7, Cul4b, Myo1e, Irs1) suggest a disruption in
396 intracellular trafficking and autophagy due to excessive ERM phosphorylation. Together,
397 these data map Ezrin interactomes in WT and LRRK2 G2019S$^{ki/ki}$ mouse cortical
398 astrocytes *in vivo*, revealing changes in Ezrin interactions with proteins involved in
399 catabolic processes and autophagy. This finding highlights a potential molecular
400 mechanism linking Lrrk2-Ezrin signaling to astrocyte morphogenesis.

401 **Atg7 is an Ezrin interactor that is required for proper astrocyte morphogenesis.**

402 Among high-confidence astrocytic Ezrin interactors, we identified autophagy-
403 related gene 7 (Atg7), a crucial autophagy regulator, which was enriched (~2.3-fold) in

404 the Ezrin-BioID fraction of WT astrocytes but less abundant (-2.0-fold) in the Ezrin-BioID
405 fraction of LRRK2 G2019S$^{ki/ki}$ astrocytes compared to the Cyto-BioID. Atg7 is essential
406 for autophagy initiation and has been implicated in neurological disorders[68,69]. However,
407 its role in astrocytes and its interaction with Ezrin is unclear. To explore this, we used
408 AlphaFold-2.0 Multimer[70] to model the structures of Ezrin and Atg7 alone or in complex.

409 Atg7, a homodimer, has two globular domains: an N-terminal domain and a C-
410 terminal domain that are separated by a short flexible linker. The C-terminal domain is
411 further divided into the adenylation and extreme C-terminal domains (Figure 7A-B)[71].
412 Ezrin has an N-terminal FERM (four-point one, Ezrin, Radixin, Moesin) domain
413 (subdivided into three subdomains: F1, F2, and F3), an α-helical domain, and a C-terminal
414 ERM Association domain (C-ERMAD) (Figure 7C)[62]. Upon phosphorylation of T567 and
415 binding to PIP2, Ezrin adopts an open conformation (Figure 7D; see Methods for details
416 of modeling)[72]. We then predicted the structure of the complex formed between the closed
417 conformation of Ezrin and the homodimer of Atg7 (Figure 7E). Alpha-fold 2.0 Multimer, in
418 conjunction with CABS-Flex 2.0 and PyMol, was used to predict and assess
419 conformational changes in Atg7 and Ezrin after binding each other (Figure 7F). When
420 Ezrin binds Atg7, it is predicted to undergo drastic conformational changes in its α-helical
421 domain, which is pulled towards the ERMAD and FERM domains, whereas the changes
422 in the Atg7 dimer structure after Ezrin binding are minimal (Figure 7F).

423 To validate the interaction between Ezrin and Atg7, we performed co-
424 immunoprecipitation (Co-IP) in HEK293T cells overexpressing Myc-tagged Atg7 (Atg7-
425 Myc) and HA-tagged WT Ezrin. To understand how the open or closed conformation of

426 Ezrin would impact the Ezrin/Atg7 interaction, we also conducted Co-IPs with modulation
427 of Ezrin phosphorylation levels: phospho-mimetic T567D ("TD", open) and phospho-dead
428 T567A ("TA", closed) Ezrin. We found that WT Ezrin or phospho-dead Ezrin
429 coimmunoprecipitated with Myc-Atg7, indicating that Atg7 interacts with WT Ezrin or
430 phospho-dead Ezrin (Figure 7G). However, the interaction between Atg7 and phospho-
431 mimetic Ezrin was significantly reduced (Figure 7H). These results support a
432 phosphorylation-dependent interaction between Ezrin and Atg7 that is consistent with our
433 BioID data showing reduced Atg7/Ezrin interaction in LRRK2 G2019S$^{ki/ki}$ astrocytes.

434 To test if Atg7 is required for astrocyte morphology, we developed a short hairpin
435 RNA (shRNA) that targets both rat and mouse *Atg7,* which effectively reduced *Atg7*
436 mRNA in mouse cells (Figure S14A). Knockdown of Atg7 in rat astrocytes significantly
437 reduced neuron-induced astrocyte morphogenesis *in vitro* in a neuron-astrocyte co-
438 culture assay (Figure S14B-C). *In vivo*, Atg7 knockdown in WT astrocytes reduced
439 astrocyte territory volume and morphological complexity, resembling the LRRK2
440 G2019S$^{ki/ki}$ astrocytes transfected with shControl (Figure 7I-K). In LRRK2 G2019S$^{ki/ki}$
441 astrocytes, Atg7 knockdown improved morphological complexity but did not further
442 reduce territory volume (Figure 7J-K). These findings highlight Atg7's role in regulating
443 astrocyte morphology and suggest its dysfunction in LRRK2 G2019S$^{ki/ki}$ astrocytes
444 contributes to altered morphology.

445 DISCUSSION

446 Here, we describe a previously unknown role for Lrrk2, a PD-linked gene, in
447 controlling astrocyte morphological complexity by regulating the phosphorylation state of

448 ERM proteins. In the presence of LRRK2 G2019S mutation, we found enhanced ERM
449 phosphorylation in human and mouse cortical astrocytes. ERM hyperphosphorylation in
450 the LRRK2 G2019S background is specific to a subset of the ACC and MOp astrocytes
451 of juvenile and adult mice. Previous studies suggested a direct interaction between
452 LRRK2 and ERM proteins[17] and that ERM proteins are substrates of LRRK2[43,44].
453 However, whether the enhanced ERM phosphorylation in LRRK2 G2019S astrocytes is
454 due to a direct effect of LRRK2 kinase is unclear. Several other kinases, such as
455 lymphocyte-oriented kinase, STE20-like protein kinase (SLK), and Rho kinase, were
456 found to be involved in ERM phosphorylation[73], suggesting the enhanced ERM
457 phosphorylation we observed in LRRK2 G2019S brains may be an indirect effect of the
458 LRRK2 G2019S mutation on the activities of these kinases.

459 **How does ERM phosphorylation control astrocyte morphology and synaptogenic**
460 **functions?**

461 The canonical function of ERM proteins is linking the actin cytoskeleton with the
462 plasma membrane, thus allowing cellular process outgrowth and morphogenesis[59]. Our
463 findings suggest that disruptions in the interaction between Ezrin and a core autophagy-
464 related protein, Atg7, contribute to the altered astrocyte morphology observed in LRRK2
465 G2019S$^{ki/ki}$ mice. *In vivo* Ezrin interactome in astrocytes included several other
466 autophagy-related proteins, which changed their proximity to Ezrin in the LRRK2
467 G2019S$^{ki/ki}$ astrocytes compared to WT astrocytes. These observations indicate that
468 dysregulated autophagy due to ERM hyperphosphorylation may underlie the deficits we
469 observed in LRRK2 G2019S$^{ki/ki}$ astrocytes.

470 Another intriguing observation is that, *in vivo*, knocking down Atg7 in WT
471 astrocytes reduces astrocyte morphological complexity. Atg7 is a homodimeric E1-like
472 enzyme essential for autophagy, which maintains cellular homeostasis by degrading and
473 recycling damaged organelles and proteins[68]. Autophagic dysregulation is linked to
474 neurodegenerative diseases, including those associated with PD-related LRRK2
475 mutations[25,74,67]. However, the role of autophagy in astrocyte morphology and
476 synaptogenic functions is not well understood, nor is the impact of LRRK2 G2019S on
477 autophagy in astrocytes. It is possible that Atg7 depletion disrupts autophagic flux,
478 causing the accumulation of damaged components that compromise astrocyte structure
479 and function.

480 Our data also show that Atg7 knockdown in LRRK2 G2019S astrocytes does not
481 worsen their morphological defects. The G2019S mutation enhances LRRK2's kinase
482 activity, leading to aberrant phosphorylation of Rab proteins that traps them on the
483 membrane surface.[75]. Our studies revealed that Atg7/Ezrin interaction requires the
484 unphosphorylated form of Ezrin. It is plausible that this interaction, which is impaired in
485 LRRK2 G2019S astrocytes, diminished Atg7 function in astrocytes. Therefore, additional
486 knockdown of Atg7 in LRRK2 G2019S$^{ki/ki}$ astrocytes does not further reduce their size
487 and complexity. Alternatively, LRRK2 G2019S$^{ki/ki}$ astrocytes may compensate by
488 upregulating other degradation pathways like ubiquitination and proteasomal degradation.
489 These mechanisms are crucial for clearing misfolded or damaged proteins in the absence
490 of functional endolysosomal function and may help mitigate the loss of autophagic flux[76,77].
491 Our Ezrin BioID dataset also showed that Nedd4l, an E3 ubiquitin ligase[78], lost proximity
492 to Ezrin in LRRK2 G2019S$^{ki/ki}$ astrocytes (Figure 6).

493 Astrocytes regulate synapse formation and function through cell adhesion
494 molecules and secreted proteins that signal to neurons[6]. Synaptogenic proteins like Hevin
495 and thrombospondins shape cortical excitatory circuits[79,80]. ERM proteins are known to
496 link the actin cytoskeleton with the plasma membrane, supporting cellular process
497 outgrowth and morphogenesis[72,81,82], but their role in secretion is less understood.
498 Phosphorylation of ERM proteins may refine secretory mechanisms in astrocytes or
499 regulate synapse elimination via phagocytosis. Supporting this possibility, a recent study
500 found that synapses were more likely to be eliminated if phospho-ERM proteins were
501 localized to peri-synaptic astrocyte processes in amyotrophic lateral sclerosis patient
502 brains and mouse models[83]. Future research exploring the relationships between Lrrk2,
503 ERM, and autophagy in astrocytes will help clarify these processes and their impact on
504 brain region-specific excitatory and inhibitory synapse phenotypes.

505 **Implications for therapeutic development**

506 LRRK2 G2019S$^{ki/ki}$ mice do not recapitulate motor symptoms of PD because there
507 is no detectable dopaminergic neuron loss in these mice[24,26]. However, these mice serve
508 as good models for the non-motor (prodromal) PD symptoms seen in LRRK2 G2019S
509 carriers[84]. These non-motor symptoms, which arise long before motor dysfunction in PD,
510 indicate aberrant synaptic connectivity within multiple brain circuits, including the cortex,
511 long before the death of dopaminergic neurons[85].

512 In agreement, LRRK2 G2019S$^{ki/ki}$ mice display early circuit dysfunction and non-
513 motor symptoms akin to prodromal PD. Previous studies showed that LRRK2 G2019S$^{ki/ki}$
514 mice have deficits in attention and goal-directed learning and differential responses to
515 stress[31-33]. Our findings showing synaptic deficits in the ACC of LRRK2 G2019S$^{ki/ki}$ mice

516 (Figure 2-3) fit well with these studies because the ACC is a brain region that controls
517 attention, goal-directed actions, and mood[86,87]. Furthermore, we observed synaptic
518 deficits in the ACC of LRRK2 G2019S$^{ki/ki}$ mice concurrently with astrocyte morphological
519 deficits located in the ACC and MOp.

520 Why do ERM phosphorylation and synaptic deficits occur in specific brain regions
521 of LRRK2 G2019S$^{ki/ki}$ mice? Cortical astrocytes are heterogeneous in their gene
522 expression, morphology, and function[88,89]. Interestingly, cortical astrocyte heterogeneity
523 is controlled by layer-specific neuron heterogeneity[88,89]. It is plausible that neurons and
524 astrocytes in different cortical regions have varying levels of LRRK2 and diverse
525 susceptibilities to LRRK2 mutations. The ACC and MOp may have a high dependence
526 on the LRRK2-ERM pathway to maintain synaptic integrity and astrocyte function. A
527 recent single-nucleus RNA sequencing in the striatum revealed that the differential
528 expression level of LRRK2 is correlated with changes in the ciliogenesis of different
529 cholinergic neurons[90], suggesting that LRRK2 transcriptional states influence cell function
530 in a cell-type-specific manner. We believe future studies investigating the impacts of
531 LRRK2 G2019S on cortical neurons and astrocytes' transcriptional profiles will explain
532 why specific brain regions and astrocyte populations are susceptible to the LRRK2
533 G2019S mutation.

534 In sum, our findings reveal a critical function for Lrrk2 in astrocyte development
535 and synaptic connectivity, suggesting that Lrrk2-mediated ERM hyperphosphorylation in
536 astrocytes is an early mediator of PD pathogenesis. This astrocytic dysfunction could
537 directly contribute to synaptic deficits observed in the prodromal stages of PD. Moreover,
538 our data indicate that restoring astrocyte function even post-development could be a

539 promising strategy for treating excitatory synaptic pathology. Identifying the molecular
540 mechanisms by which Lrrk2 controls ERM phosphorylation and the specific phosphatases
541 involved could lead to new therapeutic targets for PD.

542 **Limitations of the study**

543 In our study, we found that a subset of astrocytes in the ACC and MOp were
544 responsive to LRRK2 kinase activity. We also pinpoint that the balance of ERM
545 phosphorylation plays a crucial role in regulating astrocyte morphology in the ACC and
546 MOp. However, astrocytes display molecular, morphological, and functional
547 heterogeneities[91]. We do not yet know why these astrocytes in the ACC and MOp would
548 be sensitive to LRRK2 kinase activity and how these astrocytes are unique compared to
549 other astrocytes in terms of their transcriptional and proteomic profiles. Another future
550 direction would be to determine how the ERM phosphorylation balance modulates
551 astrocyte morphological changes and synapse changes. ERM is a crucial player in linking
552 F-actin to the cell membrane and is important for regulating membrane tension. Actin
553 cytoskeleton dynamics are important for astrocyte morphogenesis[92]. Future single-cell
554 multi-omics studies and experiments understanding how ERM phosphorylation alters
555 actin cytoskeleton dynamics in astrocytes will help us address these current limitations.
556 In addition, the difference in GFAP levels between human PD patients and LRRK2
557 G2019S$^{ki/ki}$ mice reflects the complexity of human PD pathology, the limitations of single-
558 gene mouse models, and potential species-specific differences in astrocyte reactivity.
559 This discrepancy highlights the challenges in modeling human neurodegenerative
560 diseases in animal models and underscores the need for caution when translating
561 findings from animal studies to human disease. Furthermore, in our study, we used PALE

562 to label astrocytes. While PALE is a powerful tool that allows us to label a sparse
563 population of astrocytes in the brain and study their morphological complexity in detail, it
564 has limitations in labeling astrocytes in deep brain regions like the striatum and substantia
565 pars compacta. Future studies using systemic approaches may overcome this technical
566 limitation and clarify whether and how LRRK2 G2019S affects astrocyte morphology and
567 function in additional brain regions.

568 **FIGURE LEGENDS**

569 **Figure 1: ERM phosphorylation is impaired in PD patients carrying LRRK2 G2019S**
570 **mutation.** (A) Schematic of human frontal cortex regions analyzed for phospho-ERM
571 staining. (B) Representative confocal images of GFAP (green) and phospho-ERM (purple)
572 in the frontal cortex of human controls (n = 4; 3M, 1F) and LRRK2 G2019S mutation
573 carriers (n = 3; 2M, 1F), aged >80 years. Scale bar, 200 μm. (C) Quantification of GFAP
574 integrated density in (B). GFAP: t (5) = 2.822, p = 0.037; phospho-ERM: t (5) = 5.695, p
575 = 0.0023. Grey dots: individual images; black dots: control averages; blue dots: mutation
576 carrier averages. (D) Schematic of mouse anterior cingulate cortex (ACC) and primary
577 motor cortex (MOp) analyzed for phospho-ERM staining. (E-F) Representative confocal
578 images of phospho-ERM in the ACC and the MOp of WT or LRRK2 G2019S$^{ki/ki}$ Aldh1L1-
579 eGFP mice at P21. Scale bar, 10 μm. (G-H) Representative confocal images of phospho-
580 ERM in the ACC and MOp of WT (n = 4; 2M, 2F) or LRRK2 G2019S$^{ki/ki}$ Aldh1L1-eGFP
581 mice (n = 4; 2M, 2F) at P21. Scale bar, 200 μm. (I) Quantification of phospho-ERM
582 integrated density in (G-H). For the ACC, nested t-test, unpaired two-tailed t-test. t (6) =
583 4.247, p = 0.0054. For the MOp, nested t-test, unpaired two-tailed t-test. t (6) = 2.392, p
584 = 0.0536. (J-K) Representative confocal images of phospho-ERM (purple) in the ACC

585 and MOp of WT (n = 4; 2M, 2F) or LRRK2 G2019S$^{ki/ki}$ Aldh1L1-eGFP (n = 4; 2M, 2F) mice
586 at P84. Scale bar, 200 µm. (L) Quantification of phospho-ERM integrated density in (J-K),
587 For the ACC, nested t-test, unpaired two-tailed t-test. t (6) = 4.383, p = 0.0047. For the
588 MOp, nested t-test, unpaired two-tailed t-test. t (6) = 3.898, p = 0.0080. Grey dots:
589 individual images; black dots: WT averages; blue dots: mutant averages.

590 **Figure 2: LRRK2 G2019S affects excitatory and inhibitory synapse numbers in the**
591 **ACC and MOp.** (A-B) Schematics of analyzed brain regions (ACC and MOp) and
592 methods for quantifying VGluT1-PSD95 and VGAT-GEPHYRIN colocalized puncta. (C)
593 Representative images of VGluT1-PSD95 staining in ventral ACC L1 of WT and LRRK2
594 G2019S$^{ki/ki}$ mice at P84. Scale bar, 10 µm. (D) Quantification of VGluT1-PSD95 puncta
595 in ventral ACC L1 and L2-3, normalized to WT means. n = 5/group (3M, 2F). Nested o
596 ANOVA: [F(3, 56) = 12.48, p < 0.0001]. Bonferroni's test: L1 (p < 0.0001), L2-3 (p =
597 0.0002). (E) Representative images of VGluT1-PSD95 staining in MOp L1 at P84. Scale
598 bar, 10 µm. (F) Quantification of VGluT1-PSD95 puncta in MOp L1 and L2-3. n = 5/group
599 (3M, 2F). No significant differences (Bonferroni's test: p > 0.05). (G) Representative
600 images of VGAT-GEPHYRIN staining in ventral ACC L1. Scale bar, 10 µm. (H)
601 Quantification of VGAT-GEPHYRIN puncta in ACC L1 and L2-3, normalized to WT means.
602 n = 4/group (2M, 2F). No significant differences (Bonferroni's test: p > 0.05). (I)
603 Representative images of VGAT-GEPHYRIN staining in MOp L1. Scale bar, 10 µm. (J)
604 Quantification of VGAT-GEPHYRIN puncta in MOp L1 and L2-3. n = 6/group (3M, 3F).
605 Nested one-way ANOVA: [F(3, 68) = 25.88, p < 0.0001]. Bonferroni's test: L1 (p < 0.0001),
606 L2-3 (p < 0.0001). Grey dots: individual images; black dots: WT averages; blue dots:
607 mutant averages.

608 **Figure 3: LRRK2 G2019S affects excitatory and inhibitory synapse function in the**
609 **ACC and MOp.** (A) Representative mEPSC traces from ventral ACC L2-3 pyramidal
610 neurons in WT and LRRK2 G2019S$^{ki/ki}$ mice. (B) Cumulative probability and quantification
611 of mEPSC frequency: n = 15 (WT), 13 (LRRK2 G2019S$^{ki/ki}$) neurons, 4 mice/genotype.
612 Kolmogorov-Smirnov test: D = 0.504, $p < 0.001$. Mean frequency: WT (2.878 ± 0.6355),
613 LRRK2 G2019S$^{ki/ki}$ (0.9673 ± 0.2328). Unpaired t-test: t (6) = 2.823, $p = 0.0302$. (C)
614 Cumulative probability and quantification of mEPSC amplitude: n = 14 (WT), 12 (LRRK2
615 G2019S$^{ki/ki}$) neurons. Kolmogorov-Smirnov test: D = 0.194, $p < 0.0001$. Mean amplitude:
616 WT (15.5 ± 0.6325), LRRK2 G2019S$^{ki/ki}$ (13.9 ± 0.9017). Unpaired t-test: t (6) = 1.451, p
617 = 0.197. (D) Representative mIPSC traces from MOp L2-3 pyramidal neurons in WT and
618 LRRK2 G2019S$^{ki/ki}$ mice. (E) Cumulative probability and quantification of mIPSC
619 frequency: n = 12 (WT), 11 (LRRK2 G2019S$^{ki/ki}$) neurons, 4 WT, 3 LRRK2 G2019S$^{ki/ki}$
620 mice. Kolmogorov-Smirnov test: D = 0.424, $p < 0.0001$. Mean frequency: WT (0.7788 ±
621 0.1012), LRRK2 G2019S$^{ki/ki}$ (1.301 ± 0.07291). Unpaired t-test: t (5) = 3.883, $p = 0.0116$.
622 (F) Cumulative probability and quantification of mIPSC amplitude: n = 12 (WT), 11
623 (LRRK2 G2019S$^{ki/ki}$) neurons. Kolmogorov-Smirnov test: D = 0.382, $p < 0.0001$. Mean
624 amplitude: WT (8.633 ± 0.4883), LRRK2 G2019S$^{ki/ki}$ (9.834 ± 0.5558). Unpaired t-test: t
625 (5) = 1.62, $p = 0.1662$. Data are presented as mean ± s.e.m.

626 **Figure 4: Overexpression of phospho-dead Ezrin in adult LRRK2 G2019S$^{ki/ki}$**
627 **astrocytes restores excitatory synapse number and function in the ventral ACC.** (A)
628 Representative ventral ACC images of WT and LRRK2 G2019Ski/ki mice injected with
629 AAV-HA-WT or Phospho-dead EZRIN, stained for HA and phospho-ERM (P84). Scale
630 bar, 200 µm. (B) Quantification of phospho-ERM intensity, n = 6/group (3M, 3F). One-

631 way ANOVA [F(3, 20) = 31.62, $p < 0.0001$], Bonferroni's test: significant differences
632 between WT + WT EZRIN vs. LRRK2 + WT EZRIN ($p < 0.0001$), and LRRK2 + WT EZRIN
633 vs. LRRK2 + Phospho-dead EZRIN ($p < 0.0001$). No significant differences for other
634 comparisons ($p > 0.05$). (C-D) Representative ACC L1 and L2-3 images of
635 VGluT1/PSD95 staining (P84). Scale bar, 10 µm. Quantification of co-localized puncta
636 normalized to WT + WT EZRIN (n = 5-6/group). L1: One-way ANOVA [F(3, 19) = 5.882,
637 $p = 0.0051$], Bonferroni's test: significant differences among WT + WT EZRIN, LRRK2 +
638 WT EZRIN, and their Phospho-dead counterparts ($p < 0.05$). L2-3: One-way ANOVA [F(3,
639 18) = 10.45, $p = 0.0003$], Bonferroni's test: significant group differences ($p < 0.05$). (E)
640 Representative mEPSC traces from L2-3 pyramidal neurons. (F) Synaptic event
641 frequency quantification (n = 11-15 neurons from 4 mice/group). Kruskal-Wallis test [H(3)
642 = 36.83, $p < 0.0001$], Dunn's posthoc: significant differences between WT + WT EZRIN
643 vs. all other groups ($p < 0.0001$), except LRRK2 + Phospho-dead EZRIN ($p > 0.9999$).
644 (G) Synaptic event amplitude (n = 11-15 neurons from 4 mice/group). Kruskal-Wallis test
645 [H(3) = 7.051, $p = 0.0703$]; no significant differences across groups ($p > 0.05$). Data are
646 mean ± s.e.m.

647 **Figure 5: Astrocytic LRRK2 controls astrocyte morphology by balancing ERM**
648 **phosphorylation levels *in vivo*.** (A) Representative images of ACC and MOp L2-3
649 astrocytes in WT and LRRK2 G2019S$^{ki/ki}$ (P21) expressing PB-mCherry-CAAX ±
650 Phospho-dead EZRIN. Astrocyte territory in cyan. Scale bar, 10 µm. (B) Astrocyte territory
651 volume (n = 16-18 astrocytes, 6 mice/group). One-way ANOVA [F(3, 20) = 7.987, p =
652 0.0011] with Bonferroni's test showed significant differences: WT vs. LRRK2 G2019S$^{ki/ki}$
653 (p = 0.0178), WT vs. WT + Phospho-dead EZRIN O/E (p = 0.0037), and WT + Phospho-

654 dead EZRIN O/E vs. LRRK2 G2019S$^{ki/ki}$ + Phospho-mimetic EZRIN O/E (p = 0.0165);
655 other comparisons were not significant (p > 0.05). (C) Astrocyte branching complexity (n
656 = 16-18 astrocytes, 6 mice/group). Two-way ANOVA showed main effects of condition
657 [F(2.505, 3305) = 158.4, $p < 0.0001$], radius [F(88, 1602) = 218.5, $p < 0.0001$], and their
658 interaction [F(264, 3958) = 10.62, $p < 0.0001$]. Bonferroni's test identified significant
659 differences between groups (all $p < 0.0001$), except WT vs. LRRK2 G2019S$^{ki/ki}$ +
660 Phospho-dead EZRIN O/E ($p = 0.5469$). (D) Proposed model of Ezrin conformational
661 transition and Lrrk2 regulation in astrocyte morphogenesis. (E) Images of ACC and MOp
662 L2-3 astrocytes expressing shControl-mCherry-CAAX or shLrrk2-mCherry-CAAX ±
663 Phospho-mimetic EZRIN. Scale bar, 10 µm. (F) Astrocyte territory volume (n = 18-22
664 astrocytes, 5–6 mice/group). One-way ANOVA [F(3, 19) = 5.47, $p = 0.0070$] with
665 Bonferroni's test showed significant differences between shControl and shLrrk2 ($p =$
666 0.0132), and shLrrk2 vs. shLrrk2 + Phospho-mimetic EZRIN O/E ($p = 0.0152$); no other
667 comparisons were significant ($p > 0.05$). (G) Astrocyte branching complexity (n = 16-22
668 astrocytes/group). Two-way ANOVA revealed significant main effects of condition
669 [F(2.435, 7008) = 225.0, $p < 0.0001$], radius [F(88, 8633) = 325.4, $p < 0.0001$], and their
670 interaction [F(264, 8633) = 5.908, $p < 0.0001$]. Bonferroni's test identified significant
671 differences between most groups (all $p < 0.0001$) except shControl vs. shControl +
672 Phospho-mimetic EZRIN O/E ($p > 0.9999$). Data are mean ± s.e.m.

673 **Figure 6: LRRK2 G2019S alters the interactome of astrocytic Ezrin *in vivo*.** (A)
674 Astrocyte-specific AAVs (serotype PHP.eB) were used to express Ezrin or nonspecific
675 cytosolic control. NES, nuclear export sequence; ITR, inverted terminal repeats;
676 GfaABC1D truncated GFAP promoter; HA, hemagglutinin tag; pA, polyadenylation. (B)

677 Outline of the experimental paradigm. n = 3 biological replicates/construct/genotype (1
678 replicate = 2 animals per pooled sample). (C) Volcano plot showing the differential
679 abundance of proteins detected by Astro-EZRIN-BioID in WT and LRRK2 G2019S$^{ki/ki}$
680 cortices. (D-E) Bars show the top 10 most significant Gene Ontology (GO) terms, ordered
681 by lowest adjusted p-value, for the proteins differentially detected by Astro-EZRIN-BioID
682 in WT compared to LRRK2 G2019S$^{ki/ki}$ (D) Molecular function. (E) Biological Process. (F)
683 The interaction network depicts 58 high-confidence proteins that gained or lost proximity
684 to Ezrin in LRRK2 G2019S$^{ki/ki}$ compared to WT mice. (G-H) Heatmaps depict fold-change
685 in abundance (Astro-EZRIN-BioID / Asto-Cyto-BioID) of proteins with high confidence
686 changed proximity to Ezrin in LRRK2 G2019S$^{ki/ki}$ astrocytes.

687 **Figure 7: Interaction between Atg7 and Ezrin depends on Ezrin's phosphorylation**
688 **state.** (A) Schematic of Atg7 domains. (B) Predicted Atg7 homodimer model. (C)
689 Schematic of Ezrin domains. (D) Predicted Ezrin structures in closed and open
690 conformations. (E) Predicted Atg7/Ezrin interaction. (F) Structural changes in Ezrin and
691 Atg7 upon binding. (G) Co-immunoprecipitation of Ezrin-HA by Atg7-Myc in HEK293T
692 cells expressing WT, phospho-dead, or phospho-mimetic Ezrin. Ezrin was detected with
693 anti-HA and Atg7 was detected with anti-Myc. (H) Quantification of (G). One-way ANOVA
694 [$F(2,6) = 9.932$, $p = 0.0125$] with Tukey's test: WT vs. phospho-mimetic Ezrin ($p = 0.0151$),
695 phospho-dead vs. phospho-mimetic Ezrin ($p = 0.0272$), WT vs. phospho-dead Ezrin ($p =$
696 0.8658). n = 3 experiments. (I) Images of ACC and MOp L2-3 astrocytes at P21
697 expressing shControl or shAtg7-PB-mCherry-CAAX. Scale bar, 10 µm. (J) Quantification
698 of astrocyte territories. Nested ANOVA [$F(3,28) = 9.484$, $p = 0.0002$] with Bonferroni tests:
699 WT shControl vs. LRRK2 G2019S$^{ki/ki}$ shControl ($p = 0.0036$), WT shControl vs. WT

700 shAtg7 (p = 0.0003), WT shAtg7 vs. LRRK2 G2019S$^{ki/ki}$ shAtg7 (p = 0.0109). n = 20–25
701 cells from 4–5 mice/group. (K) Astrocyte branching complexity. Two-way ANOVA
702 revealed significant condition [$F(2.324, 472.6) = 43.1$, $p < 0.05$], radius [$F(9, 250) = 301.8$,
703 $p < 0.05$], and interaction effects [$F(27, 610) = 4.539$, $p < 0.05$]. Bonferroni tests showed
704 significant differences between groups, including WT shControl vs. LRRK2 G2019S$^{ki/ki}$
705 shControl ($p < 0.0001$) and WT shControl vs. WT shAtg7 ($p < 0.0001$).

706 **STAR METHODS**

707 **KEY RESOURCES TABLE**

REAGENT or RESOURCE	SOURCE	IDENTIFIER
β-actin	Sigma-Aldrich	Cat# A5441, RRID: AB_476744
ERM	Cell Signaling	Cat# 3142, RRID:AB_2100313
GAPDH	Abcam	Cat# ab8245, RRID:AB_2107448
Gephyrin	Synaptic Systems	Cat# 147 011, RRID:AB_887717
GFAP	Agilent	Cat# Z0334, RRID:AB_10013382
GFAP	Millipore	Cat# AB5541, RRID:AB_177521
GFP	Aves labs	GFP-1020, RRID:AB_10000240
HA	Roche	Cat# 11867423001, RRID:AB_390918
L1 (ASCS4)	DSHB	Cat# ascs4, RRID:AB_528349
LRRK2	Abcam	Cat# ab133474, RRID:AB_2713963
phospho-ERM	Cell Signaling	Cat# 3141, RRID:AB_330232
phospho-ERM	Cell Signaling	Cat# 3726, RRID: AB_10560513
phospho-Rab10	Abcam	Cat# ab230261, RRID:AB_2811274
PSD-95	Innovative Research	Cat# 51-6900, RRID: AB_87705
Sox9	Millipore	Cat# AB5535, RRID:AB_2239761
VGAT	Synaptic Systems	Cat# 131 004, RRID: AB_887873
VGluT1	Synaptic Systems	Cat# 135304, RRID: AB_887878
S100β	Millipore Sigma	Cat# S2532, RRID: AB_477499
Iba1	Synaptic Systems	Cat# 234009, RRID: AB_2891282
MAP2	Thermo Fisher Scientific	Cat# 13-1500, RRID:AB_2533001
Lambda protein phosphatase	New England Biolabs	Cat# P0753L, RRID:

Bacterial and virus strains		
One Shot STBL3	Thermo Fisher	Cat# C737303
AAV PhP.eB	This paper	N/A
Chemicals, peptides, and recombinant proteins		
AraC	Sigma	Cat# C1768
B27	GIBCO	Cat# 17504044
B27 Plus	GIBCO	Cat# A3582801
BDNF	PeproTech	Cat# 450-02
Carboxypeptidase E	R&D	Cat# 3587-ZN
CNTF	PeproTech	Cat# 450-13
DMEM	GIBCO	Cat# 11960
DPBS	GIBCO	Cat# 14287
Dystroglycan	R&D	Cat# 6868-DG
Fetal Bovine Serum	Thermo Fisher	Cat# 10-437-028
Forskolin	Sigma	Cat# F6886
Glycerol	Acros Organics	Cat# AC158920010
L-Glutamine	GIBCO	Cat# 25030-081
Hydrocortisone	Sigma	Cat# H0888-5G
Insulin	Sigma	Cat# I1882
Neurobasal	GIBCO	Cat# 21103049
Neurobasal Plus	GIBCO	Cat# A3582901
Odyssey Blocking Buffer	LI-COR Biosciences	Cat# 927-40000
Opti-MEM	Thermo Fisher	Cat# 11058021
Paraformaldehyde	Electron microscopy Sciences	Cat# 19210
Pen/Strep	GIBCO	Cat# 15140
PhosSTOP™	Roche	Cat# 4906845001
Poly-D-Lysine	Sigma	Cat# P6407
Protease Inhibitor Cocktail	Roche	Cat# 4693132001
RIPA Buffer	Sigma	Cat# R0278
Sodium Pyruvate	GIBCO	Cat# 11360-070
Tissue-Tek® O.C.T. Compound	Sakura® Finetek	Cat# 4583
Triton X-100	Roche	Cat# 11332481001

Critical commercial assays		
Endo-Free Maxi Prep Kit	QIAGEN	Cat# 12362
Experimental models: cell lines		
HEK293T	ATCC	CRL-11268
Rat primary cortical neurons	This paper	N/A
Rat primary cortical astrocytes	This paper	N/A
Experimental models: organisms/strains		
Mouse: Aldh1L1-EGFP	MMRRC	RRID: MMRRC_011015-UCD
Mouse: CD1	Charles River	RRID: IMSR_CRL:022
Mouse: LRRK2 G2019S$^{ki/ki}$	Taconic	RRID: IMSR_TAC:13940
Rat: Sprague-Dawley	Charles River	001
Recombinant DNA		
pZac2.1-GfaABC1D-Ezrin WT-BioID2-HA	This paper	N/A
pZac2.1-GfaABC1D-Ezrin T567D-BioID2-HA	This paper	N/A
pZac2.1-GfaABC1D-Ezrin T567A-BioID2-HA plasmid	This paper	N/A
pLKO.1-sh*Atg7*-EGFP	This paper	N/A
pLKO.1-shControl-EGFP	This paper	N/A
pPB-CAG-sh*LRRK2*-mCherry-CAAX	This paper	N/A
pPB-CAG-sh*Atg7*-mCherry-CAAX	This paper	N/A
pPB-CAG-shControl-mCherry-CAAX	This paper	N/A
Software and algorithms		

GraphPad Prism 9	GraphPAD	https://www.graphpad.com/scientific-software/prism/
ImageJ	NIH	https://imagej.nih.gov/ij/
Puncta Analyzer	Savage et al., 2024[93]	https://github.com/Eroglu-Lab/Syn_Bot
Minhee Analysis	Kim et al., 2021[94]	https://github.com/parkgilbong/Minhee_Analysis_Pack
In vitro Sholl analysis	Tan et al., 2023[95]	https://github.com/Eroglu-Lab/In-Vitro-Sholl
Image Studio	LICOR	https://www.licor.com

RESOURCE AVAILABILITY

Lead contact

Further information and requests for resources and reagents should be directed to and will be fulfilled by the lead contacts, Shiyi Wang (shiyi.wang@duke.edu) and Cagla Eroglu (cagla.eroglu@duke.edu).

Materials availability

The reagents generated in this study are available without restriction.

Data and code availability

The data generated during this study are available at the link https://zenodo.org/records/12729032

The proteomic data is uploaded in the repository Massive (massive.ucsd.edu), accession number: MSV000095133

EXPERIMENTAL MODELS AND SUBJECT DETAILS

Animals

All mice and rats were used in accordance with the Institutional Animal Care and Use Committee (IACUC) and the Duke Division of Laboratory Animal Resources (DLAR)

725 oversight (IACUC Protocol Numbers A147-17-06 and A117-20-05). All mice and rats were
726 housed under typical day/night conditions of 12-hour cycles. LRRK2 G2019S$^{ki/ki}$ mice
727 (RRID: IMSR_TAC:13940) were obtained through Taconic. This model was generated on
728 the C57BL6/NTac background. It has been maintained on that pure background in
729 Taconic. Aldh1l1-EGFP (RRID: MMRRC_011015-UCD) mice were obtained through
730 MMRRC and backcrossed on a C57BL/6J background. Wild-type CD1 mice used for
731 PALE were purchased through Charles River Laboratories (RRID: IMSR_CRL:022).

732 Mice and rats were used for experiments as specified in the text and figure legends.
733 For all experiments, age- and sex-matched mice were randomly assigned to experimental
734 groups based on genotypes. Mice of both sexes were included in the analysis, and we
735 did not observe any influence or association of sex on the experimental outcomes.

736 **Primary cortical neuron isolation and culture**

737 Purified (glia-free) rat cortical neurons were prepared as described previously[46]. Briefly,
738 cortices from P1 rat pups of both sexes (Sprague Dawley, Charles River Laboratories,
739 SD-001) were micro-dissected, digested in papain (~7.5 units/ml) at 33°C for 45 minutes,
740 triturated in low and high ovomucoid solutions, resuspended in panning buffer (DPBS
741 (GIBCO 14287) supplemented with BSA and insulin) and passed through a 20 μm mesh
742 filter (Elko Filtering 03-20/14). Filtered cells were incubated on negative panning dishes
743 coated with Bandeiraea Simplicifolia Lectin 1 (x2), followed by goat anti-mouse IgG+IgM
744 (H+L) (Jackson ImmunoResearch 115-005-044), and goat anti-rat IgG+IgM (H+L)
745 (Jackson ImmunoResearch 112-005-044) antibodies, and then incubated on positive
746 panning dishes coated with mouse anti-L1 (ASCS4, Developmental Studies Hybridoma
747 Bank, Univ. Iowa) to bind cortical neurons. Adherent cells were collected by forceful

748 pipetting with a P1000 pipette. Isolated neurons were pelleted (11 minutes at 200 g) and
749 resuspended in serum-free neuron growth media (NGM; Neurobasal, B27 supplement,
750 2 mM L-Glutamine, 100 U/ml Pen/Strep, 1 mM sodium pyruvate, 4.2 µg/ml Forskolin,
751 50 ng/mL BDNF, and 10 ng/mL CNTF). 70,000 neurons were plated onto 12 mm glass
752 coverslips coated with 10 µg/ml poly-D-lysine (PDL, Sigma P6407) and
753 2 µg/ml laminin and incubated at 37°C in 10% CO_2. On day *in-vitro* (DIV) 2, half of the
754 media was replaced with NGM Plus (Neurobasal Plus, B27 Plus, 100 U/mL Pen/Strep,
755 1 mM sodium pyruvate, 4.2 µg/ml Forskolin, 50 ng/ml, BDNF, and 10 ng/ml CNTF) and
756 AraC (10 µM) was added to stop the growth of proliferating contaminating cells. On DIV
757 3, all the media was replaced with NGM Plus. In experiments involving lentivirus infection,
758 100 µl of supernatant containing lentivirus plus polybrene (1 µg/ml) was added to the
759 AraC NGM mixture on DIV 2 and completely washed out on DIV 3 and replaced with NGM
760 Plus containing 100 ng/ml BDNF. Neurons were fed on DIV 6 and DIV 9 by replacing half
761 of the media with NGM Plus.

762 **Primary cortical astrocyte isolation and culture**

763 **Rat astrocyte isolation and culture**

764 Rat cortical astrocytes were prepared as described previously[46]. P1 rat cortices from both
765 sexes were micro-dissected, papain digested, triturated in low and high ovomucoid
766 solutions, and resuspended in astrocyte growth media (AGM: DMEM (GIBCO 11960), 10%
767 FBS, 10 µM, hydrocortisone, 100 U/ml Pen/Strep, 2 mM L-Glutamine, 5 µg/ml Insulin,
768 1 mM Na Pyruvate, 5 µg/ml N-Acetyl-L-cysteine). Between 15-20 million cells were plated
769 on 75 mm^2 flasks (non-ventilated cap) coated with poly-D-lysine and incubated at 37°C
770 in 10% CO_2. On DIV 3, the removal of non-astrocyte cells was performed by forcefully

771 shaking closed flasks by hand for 10-15 seconds until only an adherent monolayer of
772 astrocytes remained. AraC was added to the media from DIV 5 to DIV 7 to eliminate
773 contaminating fibroblasts. On DIV 7, astrocytes were trypsinized (0.05% Trypsin-EDTA)
774 and plated into 12-well or 6-well dishes. On DIV 8, cultured rat astrocytes were transfected
775 with shRNA and/or expression plasmids using Lipofectamine LTX with Plus Reagent
776 (Thermo Scientific) per the manufacturer's protocol. Briefly, 1 µg (12-well) or 2 µg (6-well)
777 total DNA was diluted in Opti-MEM containing Plus Reagent, mixed with Opti-MEM
778 containing LTX (1:2 DNA to LTX), and incubated for 30 minutes. The transfection solution
779 was added to astrocyte cultures and incubated at 37°C for 3 hours. On DIV 10, astrocytes
780 were trypsinized, resuspended in NGM plus, plated (20,000 cells per well) onto DIV 10
781 neurons, and co-cultured for 48 hours.

782 **shRNA plasmids**

783 pLKO.1 Puro plasmids containing shRNA (pLKO.1-shRNA) against
784 mouse/rat *Lrrk2* (sh*Lrrk2*: TRCN0000322193; GGCCGAGTTGTGGATCATATT) and
785 mouse/rat *Atg7* (sh*Atg7*: TRCN0000092163; TATTATTGAGTTCAGAGCTGG) were
786 obtained from the RNAi Consortium (TRC) via Dharmacon. Two scrambled shRNA
787 sequences were generated (GTTGCTGAATGGCGGATCTAT;
788 GTTGCGGTTATGAATAGTACT) and cloned into the pLKO.1 TRC cloning vector[96]
789 according to Addgene protocols (https://www.addgene.org/protocols/plko/). To generate
790 pLKO.1 shRNA plasmids that express EGFP (pLKO.1-shRNA-EGFP), CAG-EGFP was
791 removed from pLenLox-shNL1-CAG-EGFP[97] and inserted between Kpn1 and SpeI sites
792 in pLKO.1 Puro, replacing the puromycin resistance gene. pLKO.1 shRNA mCherry
793 plasmids were generated by replacing EGFP with mCherry between KpnI and NheI sites.

794 **PiggyBac plasmids**

795 pPB-CAG-EGFP and pGLAST-PBase were a gift from Dr. Joseph Loturco[98]. To generate
796 pPB-CAG-mCherry-CAAX, mCherry-CAAX was inserted between XmaI and NotI
797 restrictions sites to replace EGFP. To insert the hU6 promoter and shRNA in pPB-CAG-
798 mCherry-CAAX, a DNA fragment containing hU6 and shRNA was amplified from pLKO.1-
799 shRNA using Phusion High-Fidelity DNA Polymerase (NEB) with primers that introduced
800 SpeI restriction sites (Forward Primer: 5'-GGACTAGTCAGGCCCGAAGGAATAGAAG-3';
801 Reverse Primer: 5'-GGACTAGTGCCAAAGTGGATCTCTGCTG-3'). PCR products were
802 purified, digested with SpeI, and ligated into pPB-CAG-mCherry-CAAX at the SpeI
803 restriction site. An analytical digest with EcoRI followed by sequencing was used to
804 confirm the orientation of the inserted DNA fragment.

805 **Ezrin plasmids**

806 pZac2.1-GfaABC1D-Lck-GCaMP6f was a gift from Dr. Baljit Khakh (Addgene plasmid
807 #52924). pZac2.1-GfaABC1D-BioID2-HA was generated by PCR of BioID2 from pAAV-
808 hSyn-BioID2-Linker-Synapsin1a-HA[99] (Forward Primer: 5'-
809 ctagcctcgagaattcaccatgttcaaaaatcttatttg-3'; Reverse Primer: 5'-
810 ccgggtcgactctagatgcgtaatccggtacatcg-3') and inserted into the EcoRI and XbaI restriction
811 sites of pZac2.1-GfaABC1D-Lck-GCaMP6f using In-Fusion cloning (TaKaRa).
812 pHJ421(pEGFP-Ezrin WT) and pHJ423 (pEGFP-Ezrin T567D) were a gift from Stephen
813 Shaw (Addgene plasmid # 20680 and # 20681). pZac2.1-GfaABC1D-Ezrin WT-BioID2-
814 HA and pZac2.1-GfaABC1D-Ezrin T567D-BioID2-HA were generated by PCR of Ezrin
815 from pHJ421 or pHJ423 (Forward Primer: 5'-ctagcctcgagaattcaccatgccgaaaccaatca-3';
816 Reverse Primer: 5'-tgaacatggtgaattccgacagggcctcgaactcg-3') and inserted into the EcoRI

817 restriction sites of pZac2.1-GfaABC1D-BioID2, respectively. To generate pZac2.1-
818 GfaABC1D-Ezrin T567A-BioID2-HA plasmid, Q5® Site-Directed Mutagenesis Kit (NEB)
819 was used with mutagenesis primers (Forward Primer: 5'-
820 CAAGTACAAGGCGCTGCGGCAGA-3'; Reverse Primer: 5'-
821 TCCCGGCCTTGCCTCATG-3')

822 **Lentivirus production and transduction**

823 Lentiviruses containing shRNA targeting vectors were produced to test the knockdown
824 efficiency of shRNA constructs in cultured primary astrocytes or to bulk transduce
825 neurons with shRNA and GFP. To produce lentivirus, HEK293T cells were transfected
826 with a pLKO.1 shRNA Puro targeting plasmid (for astrocyte transduction), an envelope
827 plasmid (VSVG), and a packaging plasmid (dR8.91) using X-tremeGENE (Roche). One
828 day after transfection, the media was replaced with AGM (for astrocyte transduction), and
829 media containing lentivirus was collected on days 2 and 3 post-transfection. To assess
830 the knockdown efficiency of shRNAs in astrocytes, rat primary astrocytes at DIV 7 were
831 plated in 6-well dishes in 2 ml of AGM. On DIV 8, 1 ml of AGM was removed, and 500 µl
832 of fresh AGM was added along with 500 µl of lentivirus-containing media and 1 µg/ml
833 polybrene. Cultured astrocytes were treated with puromycin (1 µg/ml) from DIV 10-15 to
834 select for transduced cells. Cultured astrocytes were lysed at DIV 15 for protein extraction
835 and Western blot analysis.

836 **Immunocytochemistry**

837 Astrocyte-neuron co-cultures on glass coverslips were fixed on DIV 12 with warm 4%
838 PFA for 7 minutes, washed 3 times with PBS, blocked in a blocking buffer containing 50%

839 normal goat serum (NGS) and 0.4% Triton X-100 for 30 minutes, and washed in PBS.
840 Samples were then incubated overnight at 4°C in primary antibodies diluted in blocking
841 buffer containing 10% NGS, washed with PBS, incubated in Alexa Fluor conjugated
842 secondary antibodies (Life Technologies) for 2 hours at room temperature, and washed
843 again in PBS. Coverslips were mounted onto glass slides (VWR Scientific) with
844 Vectashield mounting media containing DAPI (Vector Labs), sealed with nail polish, and
845 imaged on an AxioImager M1 (Zeiss) fluorescence microscope. Images of healthy
846 astrocytes with strong expression of fluorescent markers that did not overlap with other
847 fluorescent astrocytes were acquired at 40x magnification in red, green, and/or DAPI
848 channels using a CCD camera. Astrocyte morphological complexity was analyzed in FIJI
849 using the Sholl analysis plugin[100], as described previously[46] (https://github.com/Eroglu-
850 Lab/In-Vitro-Sholl). Statistical analyses were conducted using a custom code in R
851 (https://github.com/Eroglu-Lab/In-Vitro-Sholl). A mixed-effect model with multiple
852 comparisons made using the Tukey post-test was used for Sholl analysis to account for
853 the variability per experiment as a random effect to evaluate differences between the
854 conditions. The exact number of independent experiments and the exact number of cells
855 analyzed are indicated in the figure legend for each experiment. To ensure the health of
856 astrocyte-neuron co-cultures, the peak for the number of astrocyte intersections must be
857 greater than or equal to 25 in the control condition. We imaged non-overlapping
858 astrocytes that contained a single nucleus (DAPI stain) and expressed consistent
859 fluorescent markers and Ezrin constructs according to the experimental conditions.

860 **Postnatal astrocyte labeling by electroporation (PALE)**

861 Late P0/early P1 mice were sedated by hypothermia until anesthetized, and 1 µl
862 of plasmid DNA mixed with Fast Green Dye was injected into the lateral ventricle of one
863 hemisphere using a pulled glass pipette (Drummond). For shRNA knockdown
864 experiments in wild-type CD1 mice, the 1 µl of DNA contained 1 µg of pGLAST-PBase
865 and 1 µg of pPB-shRNA-mCherryCAAX was injected. To label astrocytes in WT
866 and LRRK2 G2019S$^{ki/ki}$ mice, the 1 µl of DNA contained 1 µg of pGLAST-PBase and 1
867 µg of pPB-mCherry-CAAX was injected per mouse.

868 For PALE-mediated overexpression of phospho-mimetic Ezrin in shRNA knockdown
869 experiments, 0.5 µg pGLAST-PBase, 0.5 µg pPB-shRNA-mCherryCAAX, and 1 µg
870 pZac2.1-GfaABC1D-Ezrin T567D-BioID2-HA were injected in a total volume of 1 µl. For
871 phospho-dead Ezrin overexpression in WT and LRRK2 G2019S$^{ki/ki}$ mice, 0.5 µg of
872 pGLAST-PBase, 0.5 µg of pZac2.1-gfaABC1D-mCherry-CAAX, and 1 µg of pZac2.1-
873 GfaABC1D-Ezrin T567A-BioID2-HA were injected in a total volume of 1 µl. Following DNA
874 injection, electrodes were oriented with the positive terminal above the frontal cortex and
875 the negative terminal below the chin, and 5 discrete 50 ms pulses of 100 V spaced
876 950 ms apart were applied. Pups were recovered on a heating pad, returned to their home
877 cage, and monitored until collection at P21. The number of mice used for each experiment
878 is indicated in the figure legends. All animals appeared healthy at the time of collection.
879 Brain sections were examined for the presence of electroporated cells before staining.

880 **Adeno-associated virus (AAV) production and administration**

881 Purified AAVs were produced as described previously[101]. Briefly, HEK293T cells were
882 transfected with pAd-DELTA F6, serotype plasmid AAV PHP.eB, and AAV plasmid
883 (pZac2.1-GfaABC1D-Ezrin-BioID2-HA or pZac2.1-GfaABC1D-Ezrin T567A-BioID2-HA).

884 Three days after transfection, cells were collected in 15 mM NaCl, 5 mM Tris-HCl, pH 8.5,
885 and lysed with repeat freeze-thaw cycles followed by treatment with Benzonase (Novagen
886 70664) at 37°C for 30 minutes. Lysed cells were pelleted by centrifugation, and the
887 supernatant, containing AAVs, was applied to an Optiprep density gradient (Sigma D1556,
888 15%, 25%, 40%, and 60%) and centrifuged at 67,000 rpm using a Beckman Ti-70 rotor
889 for 1 hour. The AAV-enriched fraction was isolated from between 40% and
890 60% iodixanol solution and concentrated by repeated washes with sterile PBS in an
891 Amicon Ultra-15 filtration unit (NMWL: 100 kDa, Millipore UFC910008) to a final volume
892 of ∼100 µl and aliquoted for storage at −80°C. 9-week-old WT or LRRK2 G2019S$^{ki/ki}$ mice
893 placed in a stereotaxic frame were anesthetized through inhalation of 1.5% isofluorane
894 gas. 10 µl of purified AAVs having a titer of ~1 x 10^{12} GC/ml was introduced into the
895 mouse brain intravenously by injection into the retro-orbital sinus. After 3 weeks at 12-
896 week-old, mice were anesthetized with 200 mg/kg Tribromoethanol (Avertin) and
897 transcardially perfused with TBS/Heparin and 4% paraformaldehyde (PFA) at room
898 temperature (RT). Harvested brains were post-fixed overnight in 4% PFA, cryoprotected
899 in 30% sucrose, and the brain blocks were prepared with O.C.T. (TissueTek) to store at
900 −80°C. 30 µm thick brain sections were obtained through cryosectioning using a Leica
901 CM3050S (Leica, Germany) vibratome and stored in a mixture of TBS and glycerol at
902 −20°C for further free-float antibody staining procedures.

903 **Immunohistochemistry on mouse brain sections**

904 Mice used for immunohistochemistry were anesthetized with 200 mg/kg Avertin and
905 perfused with TBS/Heparin and 4% PFA. Brains were collected and post-fixed in 4% PFA
906 overnight, cryoprotected in 30% sucrose, frozen in a solution containing 2 parts 30%

907 sucrose and 1-part O.C.T. (TissueTek), and stored at −80°C. Floating coronal tissue
908 sections of 30 μm, 40 μm or 100 μm thickness were collected and stored in a 1:1 mixture
909 of TBS/glycerol at −20°C. For immunostaining, sections were washed in 1x TBS
910 containing 0.2% Triton X-100 (TBST), blocked in 10% NGS diluted in TBST, and
911 incubated in primary antibody for 2-3 nights at 4°C with gentle shaking. Primary antibodies
912 used were anti-LRRK2 (Rabbit, 1:500; ab133474, Abcam), HA (Rat, 1:500; 11867423001,
913 Roche), phospho-ERM (Rabbit, 1:500; 3141, Cell Signaling), Sox9 (Rabbit, 1:500;
914 AB5535, Millipore Sigma), GFAP (Rabbit, 1:500; Z0334, Agilent DAKO), VGluT1 (Guinea
915 pig, 1:2000; 135304, Synaptic Systems), PSD95 (Rabbit, 1:300; 51-6900, Innovative
916 Research), VGAT (Guinea pig, 1:1000; 131004, Synaptic Systems), Gephyrin (Rabbit,
917 1:1000; 147011, Synaptic Systems), S100β (Mouse IgG1, 1:200; S2532, Millipore Sigma),
918 MAP2 (Mouse IgG1, 1:200; 13-1500, Thermo Fisher Scientific), and Iba1 (Chicken, 1:500;
919 234009, Synaptic Systems). For lambda protein phosphatase (λ-PPase) treatment, brain
920 sections were divided into two groups: λ-PPase treatment group and a control group.
921 Brain sections in the treatment group were incubated with λ-PPase at 30°C for 2 hours,
922 while brain sections in the control group were incubated under identical conditions without
923 the enzyme. All sections were blocked in 5% normal goat serum and 0.3% Triton X-100
924 for 1 hour at room temperature, followed by overnight incubation with primary antibodies
925 at 4°C. Following the primary incubation, sections were washed in TBST, incubated in
926 Alexa Fluor conjugated secondary antibodies diluted 1:200 (Life Technologies) for 2-3
927 hours at room temperature, washed with TBST, and mounted onto glass slides using a
928 homemade mounting media (90% Glycerol, 20 mM Tris pH 8.0, 0.5% n-Propyl gallate)
929 and sealed with nail polish. Images were acquired with an Olympus FV 3000 microscope.

930 **Immunohistochemistry on human brain sections**

931 Floating human frontal cortex sections of 40 μm thickness were obtained from Banner
932 Sun Health Research Institute in Sun City, Arizona (4 control and 3 LRRK2 G2019S
933 mutation carrier subjects). None of the control subjects had a history of dementia or
934 neurological or psychiatric disorders at the time of death (See Supplemental Table 1).
935 Informed and written consent was obtained from the donors. For immunostaining,
936 sections were washed in 1x TBS containing 0.3% Triton X-100 (TBST), blocked in 3%
937 NGS diluted in TBST, and incubated in primary antibody 2-3 nights at 4°C with shaking.
938 Primary antibodies used were GFAP (chicken, 1:250; AB5541, Millipore Sigma),
939 phospho-ERM (Rabbit, 1:250; 3726, Cell Signaling), S100β (Mouse IgG1, 1:200; S2532,
940 Millipore Sigma), and MAP2 (Mouse IgG1, 1:200; 13-1500, Thermo Fisher Scientific).
941 Following primary incubation, sections were washed in TBST, incubated in Alexa Fluor
942 conjugated secondary antibodies diluted 1:200 (Life Technologies) for 2-3 hours at room
943 temperature, washed with TBST, and mounted onto glass slides using a homemade
944 mounting media (90% Glycerol, 20 mM Tris pH 8.0, 0.5% n-Propyl gallate) and sealed
945 with nail polish.

946 **Mouse astrocyte territory volume analysis**

947 To assess the territory volume of individual astrocytes in the mouse cortex, 100 μm-thick
948 floating sections containing anterior cingulate cortex (ACC) and primary motor cortex
949 (MOp) astrocytes labeled sparsely via PALE with mCherry-CAAX were collected. High-
950 magnification images containing an entire astrocyte (50-60 μm z-stack) were acquired
951 with an Olympus FV 3000 microscope with the 60x objective. Criteria for data inclusion
952 required that the entirety of the astrocyte could be captured within a single brain section

953 and that the astrocyte was in L2-3 of the ACC or MOp. Astrocytes in which the entire
954 astrocyte could not be captured within the section or was in other layers or outside of the
955 ACC or MOp were not imaged. Imaged astrocytes were analyzed using Imaris Bitplane
956 software as described previously[46]. Briefly, surface reconstructions were generated, and
957 the Imaris Xtensions "Visualize Surface Spots" and "Convex Hull" were used to create an
958 additional surface render representing the territory of the astrocyte. The volume of each
959 territory was recorded, and astrocyte territory sizes from biological replicates were
960 analyzed across experimental conditions using a nested two-way ANOVA followed by the
961 Bonferroni posthoc test. For 3D Sholl analysis of individual PALE astrocytes, we first
962 loaded images onto Imaris and then created a surface. After generating the surface of
963 astrocytes, we created filaments using 'Add new filament (leaf icon)'. For the
964 quantification of complexity, we clicked on the gear tool on Imaris to display Sholl
965 intersections. The number of animals and cells/animals analyzed are specified in the
966 figure legend for each experiment.

967 **Mouse synapse imaging and analysis**

968 Staining, image acquisition, and analysis of synaptic density were performed as described
969 previously[102]. Synaptic staining was performed in coronal sections (30 µm thick)
970 containing the ACC and MOp from WT and LRRK2 G2019S$^{ki/ki}$ mice. To label pre and
971 postsynaptic proteins, the following antibody combinations were used: VGluT1 and
972 PSD95 (excitatory, intracortical), VGAT, and GEPHYRIN (inhibitory). High magnification
973 60x objective plus 1.64x optical zoom z-stack images containing 15 optical sections
974 spaced 0.34 µm apart were obtained using an Olympus FV 3000 inverted confocal
975 microscope. Each z-stack was converted into 5 maximum projection images (MPI), each

976 corresponding to a 1 μm section of z plane, using FIJI. Synapses were identified by the
977 colocalization of pre and postsynaptic puncta. The number of co-localized synaptic puncta
978 of excitatory intracortical (VGluT1-PSD95) and inhibitory (VGAT-GEPHYRIN) synapses
979 were obtained using the FIJI plugin Puncta Analyzer[52]. 15 MPIs were analyzed for each
980 mouse (5 MPI/tissue section, 3 tissue sections/mouse). Between 4 and 5, age- and sex-
981 matched mice/genotype/condition were analyzed for each synaptic staining combination,
982 as indicated in the figure legends. All animals appeared healthy at the time of collection.
983 No data were excluded.

984 **Cell counting, imaging, and analysis**

985 Tile scan images containing the anterior cingulated cortex (ACC) and primary motor
986 cortex (MOp) from P21 WT and LRRK2 G2019S$^{ki/ki}$; Aldh1l1-eGFP mice were acquired
987 on a confocal Leica SP8 STED microscope using the galvo scanner and 20x objective.
988 For ALDH1L1-EGFP and SOX9 double positive cell counting in the ACC and MOp, the
989 cells labeled with ALDH1L1-EGFP and SOX9 were counted by hand using the cell
990 counter tool in FIJI. 2-4 sections per brain from 3 sex- and age-matched mice/genotype
991 were analyzed.

992 **Biochemical assays**

993 **mRNA extraction and cDNA preparation**

994 Cells stored in TRIzol (15596026, Invitrogen) were thawed and resuspended in 1 mL of
995 TRIzol. After adding 200 μL of chloroform, the samples were centrifuged at 12,000 g for
996 15 minutes at 4°C. The aqueous phase was collected, and RNA was precipitated with
997 GlycoBlue Coprecipitant (AM9515, Invitrogen) and isopropanol. The RNA pellet was
998 washed with 75% ethanol, air-dried, and resuspended in 40 μL of nuclease-free water.

999 The RNA was then isolated using the Zymo Research RNA Clean & Concentrator-5 Kit
1000 (R1014, Zymo), quantified with the Qubit RNA HS Assay Kit (Q32852, Invitrogen), and
1001 diluted to equalize concentrations. Finally, cDNA libraries were generated using qScript
1002 cDNA SuperMix (101414-102, VWR) with a temperature profile of 25°C for 5 minutes,
1003 42°C for 30 minutes, and 85°C for 5 minutes, and the resulting cDNA was diluted threefold
1004 and stored at −80°C.

1005 **Real-time qPCR**

1006 cDNA samples were plated on a 96-well qPCR plate and incubated with Fast SYBR
1007 Green Master Mix (4385616, Applied Biosystems), nuclease-free water, and the forward
1008 and reverse primers of interest at a ratio of 5 µl SYBR: 3 µl water: 0.5 µl forward primer:
1009 0.5 µl reverse primer: 1 µl sample. Each sample was plated two to four times to ensure
1010 technical replicates. A control sample (water with primers and Master Mix) served as a
1011 negative control. Cycle threshold values were collected for each well and normalized to
1012 GAPDH as a housekeeping gene. The sequences of forward (F) and reverse (R) primers
1013 used (5′→ 3′) are:

1014 Atg7: (F) 5′- GTTCGCCCCCTTTAATAGTGC -3′ and (R) 5′-
1015 TGAACTCCAACGTCAAGCGG -3′

1016 **Protein extraction and western blotting**

1017 Protein was extracted from cultured rat astrocytes using membrane solubilization buffer
1018 (25 mM Tris pH 7.4, 150 mM NaCl, 1 mM $CaCl_2$, 1 mM $MgCl_2$, 0.5% NP-40, and protease
1019 inhibitors). Cultured astrocytes were washed twice with ice-cold TBS containing 1 mM
1020 $CaCl_2$ and 1 mM $MgCl_2$ and incubated on ice in membrane solubilization buffer for
1021 20 minutes with occasional agitation. Cell lysates were collected, vortexed briefly, and

1022 centrifuged at 4°C at high speed for 10 minutes to pellet non-solubilized material. The
1023 supernatant was collected and stored at −80°C.

1024 Pierce BCA Protein Assay Kit (Thermo Fisher) was used to determine protein
1025 concentration, and lysates were mixed with 4x Pierce™ Reducing Sample Buffer (Thermo
1026 Scientific) and incubated at 45°C for 45 minutes to denature proteins. 7-10 µg (cultured
1027 astrocyte lysates) of protein was loaded into Bolt™ 4–12% Bus-Tris Plus gels (Thermo
1028 Scientific) and run at 150 V for 1 hour. Proteins were transferred at 100 V to PVDF
1029 membrane (Millipore) for 1.5 hours, blocked in 5% BSA in TBST (137 mM NaCl, 2.68 mM
1030 KCl, 24.7 mM Tris-Base, 0.1% (w/v) Tween 20) for 1 hour and incubated in primary
1031 antibodies overnight at 4°C. Primary antibodies used were: anti-LRRK2 (Rabbit, 1:500;
1032 ab133474, abcam), GAPDH (mouse, 1:5000; ab8245, abcam), β-actin (mouse, 1:5000;
1033 A5441, Millipore Sigma). The next day, membranes were washed with TBST, incubated
1034 in HRP secondary antibodies (Thermo Fisher Scientific) for 2 hours, washed in TBST,
1035 and imaged on a Biorad Gel Doc imaging system. Protein levels were quantified using
1036 FIJI.

1037 **Coimmunoprecipitation**

1038 Co-immunoprecipitation assays were performed in HEK293T cells. Cells were
1039 transfected 36 hours prior to lysis with Ezrin/Atg7 cDNA using X-tremeGENE HP (Roche)
1040 and grown to 85-90% confluency. At 36 hours post-transfection, cells were rinsed with 1x
1041 PBS and collected for lysis. Cellular lysis and protein extraction was conducted via brief
1042 vortexing in chilled membrane solubilization buffer (25mM HEPES, 150mM KCl, 1.5mM
1043 MgCl2, 0.5% NP40, 10% Glycerol) in the presence of both protease (cOmplete, Roche)
1044 and phosphatase (PhosSTOP, Roche) inhibitors. Protein concentrations of cell lysates

1045 were equalized using the Pierce™ BSA Protein Assay Kit (Thermo Fisher) and
1046 CLARIOstar Plus Plate Reader (BMG Labtech). Equalized cell lysates were incubated,
1047 while rotating, with Pierce™ Anti-c-Myc Magnetic Beads (Thermo Fisher) for 6 hours at
1048 4°C. Following this incubation, the beads were washed with chilled lysis buffer. Protein
1049 samples were eluted from beads through the addition of 2x Bromophenol Blue-free
1050 Laemilli Sample Buffer and heating to 95°C for 5 minutes. Eluted protein samples were
1051 subjected to western blot analysis and quantification using a SimpleWestern Jess
1052 (ProteinSimple) automated immunoassay system with a 12-230kDa Fluorescence
1053 Separation module and associated manufacturer's protocol. Primary antibodies used for
1054 protein detection were: Anti-Myc (Rabbit, 1:40, Cell Signaling Technologies, mAb#2278)
1055 and Anti-HA (Rat, 1:20, Roche, 11867423001). Signal detection was achieved using the
1056 following fluorescently conjugated secondary antibodies at a dilution of 1:100: IRDye®
1057 680RD Goat anti-Rabbit IgG (LI-COR, 926-68071) and IRDye® 680RD Goat anti-Rat IgG
1058 (LI-COR, 926-68076). Signal quantification was conducted with the Simple Western
1059 Compass software, utilizing quantitative electropherograms of detected signals. Ezrin co-
1060 immunoprecipitation signal intensity was background-subtracted and normalized to Ezrin
1061 protein load and Atg7 IP levels for statistical analysis. Statistical analysis was performed
1062 in GraphPad Prism 9, using one-way ANOVA with Tukey's multiple comparisons test and
1063 alpha threshold of 0.05.

1064 **Protein interaction modeling**

1065 Full-length mouse Ezrin (UniProt ID: Q4KML7) and Atg7 (UniProt ID: Q9D906) were used
1066 for structure prediction in Alphafold 2.0 Multimer. The structure of Ezrin in the open
1067 conformation was generated by segmenting independently predicted Ezrin N- and C-

1068 termini and threading them onto an open ERM hinge structure using the PyMOL2
1069 molecular visualization software. To model the Ezrin/Atg7 interaction and associated
1070 conformational changes, the structures of Ezrin and the Atg7 homodimer were predicted
1071 and docked using Alphafold 2.0 Multimer. Conformational changes in the Ezrin-Atg7
1072 protein complex were assessed using PyMOL2 and CABS-flex 2.0[103]. For all predicted
1073 structure models, the highest-confidence structures, calculated via the predicted local
1074 distance difference test (pLDDT), were subjected to energy-minimization via AMBER
1075 relaxation. The resulting minimized structures were imported into PyMOL2 for
1076 representative model production.

1077 **Proteomic analysis**

1078 ***In vivo* BioID protein purification**

1079 *In vivo* BioID experiments were performed as previously described in Takano et al., 2020
1080 with modifications[104]. Genotype-matched animals (wild-type C57BL6 or LRRK2
1081 G2019S$^{ki/ki}$) were bred to produce single-genotype litters. For each genotype (WT or
1082 G2019S), 6 pups were injected with AAVs carrying Astro-Ezrin-BioID
1083 (PHP.eB.GfaABC1D-Ezrin WT-BioID2-HA) or Astro-CYTO-BioID (PHP.eB.GfaABC1D-
1084 BioID2-HA). 2 genotype-matched cortices were pooled at the time of protein isolation,
1085 yielding 3 independent replicates per BioID construct. 12 total samples (3 per genotype
1086 per construct) were subjected to LC-MS/MS and downstream analysis. WT and LRRK2
1087 G2019S$^{ki/ki}$ P0-P2 mouse pups were anesthetized by hypothermia, and 1µl of each
1088 concentrated AAV-BioID vector was injected bilaterally into the cortex using a Hamilton
1089 syringe. Pups were monitored until they recovered on a heating pad. At P18, P19, and
1090 P20, biotin was subcutaneously injected at 24 mg/kg to increase the biotinylation

1091 efficiency. At P21, the cerebral cortices were removed and stored at -80° C. For the
1092 protein purification, each cortex was lysed in a buffer containing 50 mM Tris/HCl, pH 7.5;
1093 150 mM NaCl; 1 mM EDTA; protease inhibitor mixture (Roche); and phosphatase inhibitor
1094 mixture (PhosSTOP, Roche). Next, an equal volume of buffer containing 50 mM Tris/HCl,
1095 pH 7.5; 150 mM NaCl; 1 mM EDTA; 0.4 % SDS; 2 % TritonX-100; 2 % deoxycholate;
1096 protease inhibitor mixture; and phosphatase inhibitor mixture was added to the samples,
1097 following by sonication and centrifugation at 15,000 g for 10 min. The remaining
1098 supernatant was ultracentrifuged at 100,000g for 30 minutes at 4°C. Finally, SDS
1099 detergent was added to the samples and heated at 45°C for 45 minutes. After cooling on
1100 ice, each sample was incubated with High-Capacity Streptavidin Agarose beads
1101 (ThermoFisher) at 4°C overnight. Following incubation, the beads were serially washed:
1102 1) twice with a solution containing 2% SDS; 2) twice with a buffer 1% TritonX-100, 1%
1103 deoxycholate, 25 mM LiCl; 3) twice with 1M NaCl, and finally, five times with 50 mM
1104 ammonium bicarbonate. The biotinylated proteins attached to the agarose beads were
1105 eluted in a buffer of 125 mM Tris/HCl, pH6.8; 4% SDS; 0.2% β-mercaptoethanol; 20%
1106 glycerol; 3 mM biotin at 60°C for 15 minutes.

1107 **Sample Preparation**

1108 The Duke Proteomics and Metabolomics Shared Resource (DPMSR) received 12
1109 samples (3 of each WT CYT, GS CYT, WT EZR, and GS EZR), which were kept at -80C
1110 until processing. Samples were spiked with undigested bovine casein at a total of either
1111 1 or 2 pmol as an internal quality control standard. Next, they were reduced for 15 minutes
1112 at 80°C, alkylated with 20 mM iodoacetamide for 30 minutes at room temperature, then
1113 supplemented with a final concentration of 1.2% phosphoric acid and 636 µl of S-Trap

1114 (Protifi) binding buffer (90% MeOH/100mM TEAB). Proteins were trapped on the S-Trap
1115 micro cartridge, digested using 20 ng/µL sequencing grade trypsin (Promega) for 1 hour
1116 at 47°C, and eluted using 50 mM TEAB, followed by 0.2% FA, and lastly using 50%
1117 ACN/0.2% FA. All samples were then lyophilized to dryness. Samples were resuspended
1118 in 12 µl of 1% TFA/2% acetonitrile with 12.5 fmol/µl of yeast ADH. A study pool QC (SPQC)
1119 was created by combining equal volumes of each sample.

1120 **LC-MS/MS Analysis**

1121 Quantitative LC/MS/MS was performed on 3 µL of each sample, using an MClass UPLC
1122 system (Waters Corp) coupled to a Thermo Orbitrap Fusion Lumos high resolution
1123 accurate mass tandem mass spectrometer (Thermo) equipped with a FAIMSPro device
1124 via a nanoelectrospray ionization source. Briefly, the sample was first trapped on a
1125 Symmetry C18 20 mm × 180 µm trapping column (5 µl/min at 99.9/0.1 v/v
1126 water/acetonitrile), after which the analytical separation was performed using a 1.8 µm
1127 Acquity HSS T3 C18 75 µm × 250 mm column (Waters Corp.) with a 90-minute linear
1128 gradient of 5 to 30% acetonitrile with 0.1% formic acid at a flow rate of 400
1129 nanoliters/minute (nL/minute) with a column temperature of 55C. Data collection on the
1130 Fusion Lumos mass spectrometer was performed for three difference compensation
1131 voltages (-40v, -60v, -80v). Within each CV, a data-dependent acquisition (DDA) mode
1132 of acquisition with a r = 120,000 (at m/z 200) full MS scan from m/z 375-1500 with a target
1133 AGC value of 4e5 ions was performed. MS/MS scans with HCD settings of 30% were
1134 acquired in the linear ion trap in “rapid” mode with a target AGC value of 1e4 and max fill
1135 time of 35 ms. The total cycle time for each CV was 0.66 seconds, with total cycle times
1136 of 2 seconds between like full MS scans. A 20s dynamic exclusion was employed to

1137 increase the depth of coverage. The total analysis cycle time for each sample injection
1138 was approximately 2 hours.

1139 **Quantitative Data Analysis**

1140 Following 15 total UPLC-MS/MS analyses (excluding conditioning runs, but including 3
1141 replicate SPQC samples), data were imported into Proteome Discoverer 3.0 (Thermo
1142 Scientific Inc.) and individual LCMS data files were aligned based on the accurate mass
1143 and retention time of detected precursor ions ("features") using Minora Feature Detector
1144 algorithm in Proteome Discoverer. Relative peptide abundance was measured based on
1145 peak intensities of selected ion chromatograms of the aligned features across all runs.
1146 The MS/MS data was searched against the SwissProt *M. musculus* database, a common
1147 contaminant/spiked protein database (bovine albumin, bovine casein, yeast ADH, etc.),
1148 and an equal number of reversed-sequence "decoys" for false discovery rate
1149 determination. Sequest with INFERYS was utilized to produce fragment ion spectra and
1150 to perform the database searches. Database search parameters included fixed
1151 modification on Cys (carbamidomethyl) and variable modification on Met (oxidation).
1152 Search tolerances were 2 ppm precursor and 0.8 Da product ion with full trypsin enzyme
1153 rules. Peptide Validator and Protein FDR Validator nodes in Proteome Discoverer were
1154 used to annotate the data at a maximum 1% protein false discovery rate based on q-
1155 value calculations. Note that peptide homology was addressed using razor rules in which
1156 a peptide matched to multiple different proteins was exclusively assigned to the protein
1157 has more identified peptides. Protein homology was addressed by grouping proteins that
1158 had the same set of peptides to account for their identification. A master protein within a
1159 group was assigned based on % coverage.

1160 Prior to normalization, a filter was applied such that a peptide was removed if it was not
1161 measured at least twice across all samples and in at least 50% of the replicates in any
1162 one single group. After that filter, samples were total intensity normalized (total intensity
1163 of all peptides for a sample are summed and then normalized across all samples). Next,
1164 the following imputation strategy is applied to missing values. If less than half of the values
1165 are missing in a biological group, values are imputed with an intensity derived from a
1166 normal distribution of all values defined by measured values within the same intensity
1167 range (20 bins). If greater than half values are missing for a peptide in a group and a
1168 peptide intensity is > 5e6, then it was concluded that the peptide was misaligned and its
1169 measured intensity is set to 0. All remaining missing values are imputed with the lowest
1170 2% of all detected values. Peptide intensities were then subjected to a trimmed-mean
1171 normalization in which the top and bottom 10% of the signals were excluded, and the
1172 average of the remaining values was used to normalize across all samples. Lastly, all
1173 peptides belonging to the same protein were then summed into a single intensity. These
1174 normalized protein level intensities are what was used for the remainder of the analysis.

1175 To assess technical reproducibility, we calculated the % coefficient of variation (%CV) for
1176 each protein across 3 injections of an SPQC pool that were interspersed throughout the
1177 study (Table S4). The mean %CV of the SPQC pools was 11.7%, which is well within our
1178 expected analytical tolerances. To assess biological and technical variability, %CVs were
1179 measured for each protein across the individual groups which averaged 19.8%, which is
1180 also within our normal tolerances and indicated a reproducible IP and sample processing.

1181 As an initial statistical analysis, we calculated fold-changes between various sample
1182 groups based on the protein expression values and calculated two-tailed heteroscedastic

1183 t-test on log2-transformed data for this comparison. Those fold changes and p-values are
1184 presented for all proteins in Tables S5, S7, S9, and S10. False Discovery Rate (FDR)
1185 correction was performed using the Benjamini-Hochberg procedure, and these values are
1186 reported ("p.adjusted") in Tables S5, S7, S9, and S10. To optimize for discovery, we opted
1187 to use the less stringent parameter of unadjusted p-value for downstream analyses.
1188 Within supplemental tables, we have labeled proteins significantly more abundant ("Up",
1189 fold change >1.5 and unadjusted p-value <0.05), or less abundant ("Down", fold change
1190 >-1.5 and unadjusted p-value <0.05) in a particular genotype or BioID sample group.
1191 These annotated proteins were used for downstream analyses, including protein
1192 interaction networks using Cytoscape (v.3.9.1) and Gene Ontology (GO) enrichment
1193 analysis using the ClusterProfiler package for R, with all M. musculus genes as the
1194 reference background.

1195 **Mouse brain slice electrophysiology**

1196 For whole-cell patch-clamp recordings, 3-4 mice of each genotype and condition were
1197 used for miniature excitatory postsynaptic current (mEPSC) and miniature inhibitory
1198 postsynaptic current (mIPSC) measurements. WT and *LRRK2* G2019S$^{ki/ki}$ mice of both
1199 sexes were anesthetized with 200 mg/kg tribromoethanol (avertin) and decapitated. After
1200 decapitation, the brains were immersed in ice-cold artificial cerebrospinal fluid (aCSF, in
1201 mM): 125 NaCl, 2.5 KCl, 3 mM $MgCl_2$, 0.1 mM $CaCl_2$, 10 glucose, 25 $NaHCO_3$, 1.25
1202 $NaHPO_4$, 0.4 L-ascorbic acid, and 2 Na-pyruvate, pH 7.3-7.4 (310 mOsmol). 350 µm thick
1203 coronal slices containing the ACC were obtained using a vibrating tissue slicer (Leica
1204 VT1200; Leica Biosystems). Slices were immediately transferred to standard aCSF (33°C,
1205 continuously bubbled with 95% O_2 – 5% CO_2) containing the same as the low-calcium

1206 aCSF but with 1 mM $MgCl_2$ and 1-2 mM $CaCl_2$. After 30-minute incubation at 33°C, slices
1207 were transferred to a holding chamber with the same extracellular buffer at room
1208 temperature (RT: ~25°C). Brain slices were visualized by an upright microscope (BX61WI,
1209 Olympus) through a 40x water-immersion objective equipped with infrared-differential
1210 interference contrast optics in combination with a digital camera (ODA-IR2000WCTRL).
1211 Patch-clamp recordings were performed by using an EPC 10 patch-clamp amplifier,
1212 controlled by Patchmaster Software (HEKA). Data were acquired at a sampling rate of 50
1213 kHz and low-pass filtered at 6 kHz.

1214 To measure mEPSCs, the internal solution contained the following (in mM): 125 K-
1215 gluconate, 10 NaCl, 10 HEPES, 0.2 EGTA, 4.5 MgATP, 0.3 NaGTP, and 10 Na-
1216 phosphocreatine, pH adjusted to 7.2 – 7.4 with KOH and osmolality set to ~300 mOsmol.
1217 mEPSCs were measured in the aCSF bath solution containing 1 μM tetrodotoxin and 50
1218 μM Picrotoxin at -70 mV in voltage-clamp mode. To measure mIPSCs, the internal
1219 solution contained the following (in mM): 77 K-gluconate, 77 KCl, 10 HEPES, 0.2 EGTA,
1220 4.5 MgATP, 0.3 NaGTP, and 10 Na-phosphocreatine, pH adjusted to 7.2 – 7.4 with KOH
1221 and osmolality set to ~300 mOsmol. mIPSCs were measured in the aCSF bath solution
1222 containing 1 μM tetrodotoxin and 10 μM 6-cyano-7-nitroquinoxaline-2,3-dione (CNQX),
1223 and 50 μM D-2-amino-5-phosphonopentanoate (D-AP5) at -70 mV in voltage-clamp
1224 mode. mEPSCs and mIPSCs recorded at -70 mV were detected using Minhee Analysis
1225 software (https://github.com/parkgilbong/Minhee_Analysis_Pack). To analyze the
1226 frequency, events were counted over 5 minutes of recording. To obtain the average
1227 events for each cell, at least 100 non-overlapping events were detected and averaged.

1228 The peak amplitude of the average mEPSCs was measured relative to the baseline
1229 current.

1230 **Quantification and statistical analysis**

1231 All statistical analyses were performed in GraphPad Prism 9. Exact value of n, what n
1232 represents, and specific statistical tests for each experiment are indicated in the figure
1233 legend for each experiment. All data are represented as mean ± standard error of the
1234 mean, and data points are shown where applicable. Exact *P*-values are listed in the figure
1235 for each experiment. Where indicated, the unpaired two-tailed t-tests were run using
1236 Welch`s correction, and a correction for multiple comparisons was applied using Hom-
1237 Sidak method with an alpha threshold of 0.05 for adjusted *P*-value. A Geisser-
1238 Greenhouse correction was used for both One-way and Two-way ANOVA analyses. For
1239 Sholl analysis, statistical analyses were conducted using a custom code in R
1240 (https://github.com/Eroglu-Lab/In-Vitro-Sholl). A mixed-effect model with multiple
1241 comparisons made using the Tukey post-test was used for Sholl analysis to account for
1242 the variability per experiment as a random effect to evaluate differences between the
1243 conditions. Sample sizes were determined based on previous experience for each
1244 experiment to yield high power to detect specific effects. No statistical methods were used
1245 to predetermine the sample size. All experimental animals that appeared healthy at the
1246 time of tissue collection were processed for data collection.

1247 **ACKNOWLEDGMENTS**

1248 We thank Drs. Amy Lee, Zhiyong Liu, Nicole Calakos, Katja Brose, and Andrew Singleton
1249 for critical feedback on the manuscript. We thank Adam Okinaga and Donna Porter for
1250 their excellent technical help. This work was supported by a Foerster Bernstein Women
1251 In STEM Postdoctoral Fellowship to SW; a Chan Zuckerberg Initiative,
1252 Neurodegeneration Challenge Network Collaborative grant (DAF2018-191999 and
1253 DAF2021-237435) to CE and ARLS; the N.I.H. grants R35-NS122140 to A.R.L.S. and
1254 R01-NS102237 to CE; the Michael J. Fox Foundation for Parkinson's Research (MJFF)
1255 Astrocyte Biology in PD pilot grant (MJFF 17914 to CE and ARLS); and the joint efforts
1256 of MJFF and the Aligning Science Across Parkinson's (ASAP) initiative. MJFF administers
1257 the grant [ASAP-020607 to CE and SHS] on behalf of ASAP and the Michael J. Fox
1258 Foundation. Dr. Cagla Eroglu is an HHMI Investigator. We are grateful to the Banner Sun
1259 Health Research Institute Brain and Body Donation Program of Sun City, Arizona for the
1260 provision of human biological materials. The Brain and Body Donation Program has been
1261 supported by the National Institute of Neurological Disorders and Stroke (U24 NS072026
1262 National Brain and Tissue Resource for Parkinson's Disease and Related Disorders), the
1263 National Institute on Aging (P30AG19610 and P30AG072980, Arizona Alzheimer's
1264 Disease Center), the Arizona Biomedical Research Commission contracts 4001, 0011,
1265 05-901 and 1001 to the Arizona Parkinson's Disease Consortium and the Michael J. Fox
1266 Foundation for Parkinson's Research.

1267

IP RIGHTS NOTICE

This article is subject to HHMI's Open Access to Publications policy. HHMI lab heads have previously granted a nonexclusive CC BY 4.0 license to the public and a sublicensable license to HHMI in their research articles. Pursuant to those licenses, the author-accepted manuscript of this article can be made freely available under a CC BY 4.0 license immediately upon publication.

AUTHOR CONTRIBUTIONS

Conceptualization, SW, ARLS, and CE; Methodology, SW, RB, GS, DSB, LV, KS, JM, CXT, TT, MPR, KD, NB, LB, SHS, and CE; Investigation, SW, RB, GS, and LV; Formal analysis, SW, RB, GS, and LV; Resources, CXT, MPR, and KS; Writing – original draft, SW and CE; Writing – Review & Editing, SW, RL, and CE; Funding Acquisition, SW, SHS, ARLS, and CE.

DECLARATION OF INTERESTS

The authors declare no competing interests.

DATA AVAILABILITY

The data generated during this study are available at the link https://zenodo.org/records/12729032

The proteomic data is uploaded in the repository Massive (massive.ucsd.edu), accession number: MSV000095133

CODE AVAILABILITY

The code used to analyze Sholl data is available via the link https://github.com/Eroglu-Lab/Sholl_Macro.

1291 **REFERENCES**

1292 1 Semyanov, A. & Verkhratsky, A. Astrocytic processes: from tripartite synapses to
1293 the active milieu. *Trends Neurosci* **44**, 781-792 (2021).
1294 https://doi.org:10.1016/j.tins.2021.07.006

1295 2 Allen, N. J. & Eroglu, C. Cell Biology of Astrocyte-Synapse Interactions. *Neuron*
1296 **96**, 697-708 (2017). https://doi.org:10.1016/j.neuron.2017.09.056

1297 3 Clavreul, S. *et al.* Cortical astrocytes develop in a plastic manner at both clonal
1298 and cellular levels. *Nat Commun* **10**, 4884 (2019).
1299 https://doi.org:10.1038/s41467-019-12791-5

1300 4 Torres-Ceja, B. & Olsen, M. L. A closer look at astrocyte morphology:
1301 Development, heterogeneity, and plasticity at astrocyte leaflets. *Curr Opin*
1302 *Neurobiol* **74**, 102550 (2022). https://doi.org:10.1016/j.conb.2022.102550

1303 5 Farizatto, K. L. G. & Baldwin, K. T. Astrocyte-synapse interactions during brain
1304 development. *Curr Opin Neurobiol* **80**, 102704 (2023).
1305 https://doi.org:10.1016/j.conb.2023.102704

1306 6 Tan, C. X. & Eroglu, C. Cell adhesion molecules regulating astrocyte-neuron
1307 interactions. *Curr Opin Neurobiol* **69**, 170-177 (2021).
1308 https://doi.org:10.1016/j.conb.2021.03.015

1309 7 Holt, L. M. *et al.* Astrocyte morphogenesis is dependent on BDNF signaling via
1310 astrocytic TrkB.T1. *Elife* **8** (2019). https://doi.org:10.7554/eLife.44667

1311 8 Kam, T. I., Hinkle, J. T., Dawson, T. M. & Dawson, V. L. Microglia and astrocyte
1312 dysfunction in parkinson's disease. *Neurobiol Dis* **144**, 105028 (2020).
1313 https://doi.org:10.1016/j.nbd.2020.105028

1314 9 Brandebura, A. N., Paumier, A., Onur, T. S. & Allen, N. J. Astrocyte contribution
1315 to dysfunction, risk and progression in neurodegenerative disorders. *Nat Rev*
1316 *Neurosci* (2022). https://doi.org:10.1038/s41583-022-00641-1
1317 10 Gilks, W. P. *et al.* A common LRRK2 mutation in idiopathic Parkinson's disease.
1318 *Lancet* **365**, 415-416 (2005). https://doi.org:10.1016/S0140-6736(05)17830-1
1319 11 Benamer, H. T. The ancestry of LRRK2 Gly2019Ser parkinsonism. *Lancet Neurol*
1320 **7**, 769-770; author reply 770-761 (2008). https://doi.org:10.1016/S1474-
1321 4422(08)70178-9
1322 12 Pang, S. Y. *et al.* LRRK2, GBA and their interaction in the regulation of
1323 autophagy: implications on therapeutics in Parkinson's disease. *Transl*
1324 *Neurodegener* **11**, 5 (2022). https://doi.org:10.1186/s40035-022-00281-6
1325 13 Ren, C. *et al.* G2019S Variation in LRRK2: An Ideal Model for the Study of
1326 Parkinson's Disease? *Front Hum Neurosci* **13**, 306 (2019).
1327 https://doi.org:10.3389/fnhum.2019.00306
1328 14 Belarbi, S. *et al.* LRRK2 G2019S mutation in Parkinson's disease: a
1329 neuropsychological and neuropsychiatric study in a large Algerian cohort.
1330 *Parkinsonism Relat Disord* **16**, 676-679 (2010).
1331 https://doi.org:10.1016/j.parkreldis.2010.09.003
1332 15 West, A. B. *et al.* Parkinson's disease-associated mutations in leucine-rich repeat
1333 kinase 2 augment kinase activity. *Proc Natl Acad Sci U S A* **102**, 16842-16847
1334 (2005). https://doi.org:10.1073/pnas.0507360102

1335 16 Greggio, E. *et al.* Kinase activity is required for the toxic effects of mutant
1336 LRRK2/dardarin. *Neurobiol Dis* **23**, 329-341 (2006).
1337 https://doi.org:10.1016/j.nbd.2006.04.001
1338 17 Jaleel, M. *et al.* LRRK2 phosphorylates moesin at threonine-558: characterization
1339 of how Parkinson's disease mutants affect kinase activity. *Biochem J* **405**, 307-
1340 317 (2007). https://doi.org:10.1042/BJ20070209
1341 18 Ito, G. *et al.* Phos-tag analysis of Rab10 phosphorylation by LRRK2: a powerful
1342 assay for assessing kinase function and inhibitors. *Biochem J* **473**, 2671-2685
1343 (2016). https://doi.org:10.1042/BCJ20160557
1344 19 Steger, M. *et al.* Systematic proteomic analysis of LRRK2-mediated Rab GTPase
1345 phosphorylation establishes a connection to ciliogenesis. *Elife* **6** (2017).
1346 https://doi.org:10.7554/eLife.31012
1347 20 Steger, M. *et al.* Phosphoproteomics reveals that Parkinson's disease kinase
1348 LRRK2 regulates a subset of Rab GTPases. *Elife* **5** (2016).
1349 https://doi.org:10.7554/eLife.12813
1350 21 Kluss, J. H., Mamais, A. & Cookson, M. R. LRRK2 links genetic and sporadic
1351 Parkinson's disease. *Biochem Soc Trans* **47**, 651-661 (2019).
1352 https://doi.org:10.1042/BST20180462
1353 22 Monfrini, E. & Di Fonzo, A. Leucine-Rich Repeat Kinase (LRRK2) Genetics and
1354 Parkinson's Disease. *Adv Neurobiol* **14**, 3-30 (2017). https://doi.org:10.1007/978-
1355 3-319-49969-7_1

1356 23 Mestre, T. A. *et al.* Clustering of motor and nonmotor traits in leucine-rich repeat
1357 kinase 2 G2019S Parkinson's disease nonparkinsonian relatives: A multicenter
1358 family study. *Mov Disord* **33**, 960-965 (2018). https://doi.org:10.1002/mds.27272
1359 24 Chang, E. E. S. *et al.* LRRK2 mutant knock-in mouse models: therapeutic
1360 relevance in Parkinson's disease. *Translational Neurodegeneration* **11** (2022).
1361 https://doi.org:10.1186/s40035-022-00285-2
1362 25 Yue, M. *et al.* Progressive dopaminergic alterations and mitochondrial
1363 abnormalities in LRRK2 G2019S knock-in mice. *Neurobiol Dis* **78**, 172-195
1364 (2015). https://doi.org:10.1016/j.nbd.2015.02.031
1365 26 Longo, F. *et al.* Age-dependent dopamine transporter dysfunction and Serine129
1366 phospho-alpha-synuclein overload in G2019S LRRK2 mice. *Acta Neuropathol*
1367 *Commun* **5**, 22 (2017). https://doi.org:10.1186/s40478-017-0426-8
1368 27 Narayanan, N. S., Rodnitzky, R. L. & Uc, E. Y. Prefrontal dopamine signaling and
1369 cognitive symptoms of Parkinson's disease. *Rev Neurosci* **24**, 267-278 (2013).
1370 https://doi.org:10.1515/revneuro-2013-0004
1371 28 Cousineau, J., Plateau, V., Baufreton, J. & Le Bon-Jego, M. Dopaminergic
1372 modulation of primary motor cortex: From cellular and synaptic mechanisms
1373 underlying motor learning to cognitive symptoms in Parkinson's disease.
1374 *Neurobiol Dis* **167**, 105674 (2022). https://doi.org:10.1016/j.nbd.2022.105674
1375 29 Volta, M. & Melrose, H. LRRK2 mouse models: dissecting the behavior, striatal
1376 neurochemistry and neurophysiology of PD pathogenesis. *Biochem Soc Trans*
1377 **45**, 113-122 (2017). https://doi.org:10.1042/BST20160238

1378 30 Vingill, S., Connor-Robson, N. & Wade-Martins, R. Are rodent models of
1379 Parkinson's disease behaving as they should? *Behav Brain Res* **352**, 133-141
1380 (2018). https://doi.org:10.1016/j.bbr.2017.10.021
1381 31 Hussein, A., Tielemans, A., Baxter, M. G., Benson, D. L. & Huntley, G. W.
1382 Cognitive deficits and altered cholinergic innervation in young adult male mice
1383 carrying a Parkinson's disease Lrrk2(G2019S) knockin mutation. *Exp Neurol* **355**,
1384 114145 (2022). https://doi.org:10.1016/j.expneurol.2022.114145
1385 32 Guevara, C. A. *et al.* LRRK2 mutation alters behavioral, synaptic, and
1386 nonsynaptic adaptations to acute social stress. *J Neurophysiol* **123**, 2382-2389
1387 (2020). https://doi.org:10.1152/jn.00137.2020
1388 33 Matikainen-Ankney, B. A. *et al.* Parkinson's Disease-Linked LRRK2-G2019S
1389 Mutation Alters Synaptic Plasticity and Promotes Resilience to Chronic Social
1390 Stress in Young Adulthood. *J Neurosci* **38**, 9700-9711 (2018).
1391 https://doi.org:10.1523/JNEUROSCI.1457-18.2018
1392 34 Chen, C. *et al.* Pathway-specific dysregulation of striatal excitatory synapses by
1393 LRRK2 mutations. *Elife* **9** (2020). https://doi.org:10.7554/eLife.58997
1394 35 Kuhlmann, N. & Milnerwood, A. J. A Critical LRRK at the Synapse? The
1395 Neurobiological Function and Pathophysiological Dysfunction of LRRK2. *Front*
1396 *Mol Neurosci* **13**, 153 (2020). https://doi.org:10.3389/fnmol.2020.00153
1397 36 Lim, J. *et al.* LRRK2 G2019S Induces Anxiety/Depression-like Behavior before
1398 the Onset of Motor Dysfunction with 5-HT(1A) Receptor Upregulation in Mice. *J*
1399 *Neurosci* **38**, 1611-1621 (2018). https://doi.org:10.1523/JNEUROSCI.4051-
1400 15.2017

1401 37 Arbez, N. *et al.* G2019S-LRRK2 mutation enhances MPTP-linked Parkinsonism
1402 in mice. *Hum Mol Genet* **29**, 580-590 (2020). https://doi.org:10.1093/hmg/ddz271
1403 38 Skiteva, O., Yao, N., Sitzia, G. & Chergui, K. LRRK2-G2019S mice display
1404 alterations in glutamatergic synaptic transmission in midbrain dopamine neurons.
1405 *J Neurochem* **161**, 158-172 (2022). https://doi.org:10.1111/jnc.15588
1406 39 Lavialle, M. *et al.* Structural plasticity of perisynaptic astrocyte processes involves
1407 ezrin and metabotropic glutamate receptors. *Proc Natl Acad Sci U S A* **108**,
1408 12915-12919 (2011). https://doi.org:10.1073/pnas.1100957108
1409 40 Derouiche, A., Anlauf, E., Aumann, G., Muhlstadt, B. & Lavialle, M. Anatomical
1410 aspects of glia-synapse interaction: the perisynaptic glial sheath consists of a
1411 specialized astrocyte compartment. *J Physiol Paris* **96**, 177-182 (2002).
1412 https://doi.org:10.1016/s0928-4257(02)00004-9
1413 41 Bretscher, A., Edwards, K. & Fehon, R. G. ERM proteins and merlin: integrators
1414 at the cell cortex. *Nat Rev Mol Cell Biol* **3**, 586-599 (2002).
1415 https://doi.org:10.1038/nrm882
1416 42 Gautreau, A., Louvard, D. & Arpin, M. Morphogenic effects of ezrin require a
1417 phosphorylation-induced transition from oligomers to monomers at the plasma
1418 membrane. *J Cell Biol* **150**, 193-203 (2000). https://doi.org:10.1083/jcb.150.1.193
1419 43 Parisiadou, L. *et al.* Phosphorylation of ezrin/radixin/moesin proteins by LRRK2
1420 promotes the rearrangement of actin cytoskeleton in neuronal morphogenesis. *J*
1421 *Neurosci* **29**, 13971-13980 (2009). https://doi.org:10.1523/JNEUROSCI.3799-
1422 09.2009

1423 44 Parisiadou, L. & Cai, H. LRRK2 function on actin and microtubule dynamics in
1424 Parkinson disease. *Commun Integr Biol* **3**, 396-400 (2010).
1425 https://doi.org:10.4161/cib.3.5.12286
1426 45 Matikainen-Ankney, B. A. *et al.* Altered Development of Synapse Structure and
1427 Function in Striatum Caused by Parkinson's Disease-Linked LRRK2-G2019S
1428 Mutation. *J Neurosci* **36**, 7128-7141 (2016).
1429 https://doi.org:10.1523/JNEUROSCI.3314-15.2016
1430 46 Stogsdill, J. A. *et al.* Astrocytic neuroligins control astrocyte morphogenesis and
1431 synaptogenesis. *Nature* **551**, 192-197 (2017).
1432 https://doi.org:10.1038/nature24638
1433 47 Sofroniew, M. V. & Vinters, H. V. Astrocytes: biology and pathology. *Acta*
1434 *Neuropathol* **119**, 7-35 (2010). https://doi.org:10.1007/s00401-009-0619-8
1435 48 Hol, E. M. & Pekny, M. Glial fibrillary acidic protein (GFAP) and the astrocyte
1436 intermediate filament system in diseases of the central nervous system. *Curr*
1437 *Opin Cell Biol* **32**, 121-130 (2015). https://doi.org:10.1016/j.ceb.2015.02.004
1438 49 Skelton, P. D., Tokars, V. & Parisiadou, L. LRRK2 at Striatal Synapses: Cell-
1439 Type Specificity and Mechanistic Insights. *Cells* **11** (2022).
1440 https://doi.org:10.3390/cells11010169
1441 50 Fremeau, R. T., Jr. *et al.* The expression of vesicular glutamate transporters
1442 defines two classes of excitatory synapse. *Neuron* **31**, 247-260 (2001).
1443 https://doi.org:10.1016/s0896-6273(01)00344-0
1444 51 Micheva, K. D., Busse, B., Weiler, N. C., O'Rourke, N. & Smith, S. J. Single-
1445 synapse analysis of a diverse synapse population: proteomic imaging methods

1446 and markers. *Neuron* **68**, 639-653 (2010).
1447 https://doi.org:10.1016/j.neuron.2010.09.024
1448 52 Ippolito, D. M. & Eroglu, C. Quantifying synapses: an immunocytochemistry-
1449 based assay to quantify synapse number. *J Vis Exp* (2010).
1450 https://doi.org:10.3791/2270
1451 53 Glasgow, S. D., McPhedrain, R., Madranges, J. F., Kennedy, T. E. & Ruthazer,
1452 E. S. Approaches and Limitations in the Investigation of Synaptic Transmission
1453 and Plasticity. *Front Synaptic Neurosci* **11**, 20 (2019).
1454 https://doi.org:10.3389/fnsyn.2019.00020
1455 54 Matsuzaki, M. *et al.* Dendritic spine geometry is critical for AMPA receptor
1456 expression in hippocampal CA1 pyramidal neurons. *Nat Neurosci* **4**, 1086-1092
1457 (2001). https://doi.org:10.1038/nn736
1458 55 Zhang, Y. *et al.* An RNA-sequencing transcriptome and splicing database of glia,
1459 neurons, and vascular cells of the cerebral cortex. *J Neurosci* **34**, 11929-11947
1460 (2014). https://doi.org:10.1523/JNEUROSCI.1860-14.2014
1461 56 Zhu, L. *et al.* High turnover of ezrin T567 phosphorylation: conformation, activity,
1462 and cellular function. *Am J Physiol Cell Physiol* **293**, C874-884 (2007).
1463 https://doi.org:10.1152/ajpcell.00111.2007
1464 57 Chua, C. E. L. & Tang, B. L. Rab 10-a traffic controller in multiple cellular
1465 pathways and locations. *J Cell Physiol* **233**, 6483-6494 (2018).
1466 https://doi.org:10.1002/jcp.26503

1467 58 Fievet, B. T. *et al.* Phosphoinositide binding and phosphorylation act sequentially
1468 in the activation mechanism of ezrin. *J Cell Biol* **164**, 653-659 (2004).
1469 https://doi.org:10.1083/jcb.200307032
1470 59 Yin, L. M. & Schnoor, M. Modulation of membrane-cytoskeleton interactions:
1471 ezrin as key player. *Trends Cell Biol* **32**, 94-97 (2022).
1472 https://doi.org:10.1016/j.tcb.2021.09.005
1473 60 Heiska, L. *et al.* Association of ezrin with intercellular adhesion molecule-1 and -2
1474 (ICAM-1 and ICAM-2). Regulation by phosphatidylinositol 4, 5-bisphosphate. *J*
1475 *Biol Chem* **273**, 21893-21900 (1998). https://doi.org:10.1074/jbc.273.34.21893
1476 61 Zaman, R. *et al.* Effector-mediated ERM activation locally inhibits RhoA activity to
1477 shape the apical cell domain. *J Cell Biol* **220** (2021).
1478 https://doi.org:10.1083/jcb.202007146
1479 62 Tsai, F. C. *et al.* Ezrin enrichment on curved membranes requires a specific
1480 conformation or interaction with a curvature-sensitive partner. *Elife* **7** (2018).
1481 https://doi.org:10.7554/eLife.37262
1482 63 Matsui, T. *et al.* Rho-kinase phosphorylates COOH-terminal threonines of
1483 ezrin/radixin/moesin (ERM) proteins and regulates their head-to-tail association.
1484 *J Cell Biol* **140**, 647-657 (1998). https://doi.org:10.1083/jcb.140.3.647
1485 64 Shani, V. *et al.* Physiological and pathological roles of LRRK2 in the nuclear
1486 envelope integrity. *Hum Mol Genet* **28**, 3982-3996 (2019).
1487 https://doi.org:10.1093/hmg/ddz245

1488 65 Heaton, G. R. *et al.* Sequential screening nominates the Parkinson's disease
1489 associated kinase LRRK2 as a regulator of Clathrin-mediated endocytosis.
1490 *Neurobiol Dis* **141**, 104948 (2020). https://doi.org:10.1016/j.nbd.2020.104948
1491 66 Soto, J. S. *et al.* Astrocyte-neuron subproteomes and obsessive-compulsive
1492 disorder mechanisms. *Nature* **616**, 764-773 (2023).
1493 https://doi.org:10.1038/s41586-023-05927-7
1494 67 Plowey, E. D., Cherra, S. J., 3rd, Liu, Y. J. & Chu, C. T. Role of autophagy in
1495 G2019S-LRRK2-associated neurite shortening in differentiated SH-SY5Y cells. *J*
1496 *Neurochem* **105**, 1048-1056 (2008). https://doi.org:10.1111/j.1471-
1497 4159.2008.05217.x
1498 68 Mizushima, N. *et al.* A protein conjugation system essential for autophagy.
1499 *Nature* **395**, 395-398 (1998). https://doi.org:10.1038/26506
1500 69 Collier, J. J. *et al.* Developmental Consequences of Defective ATG7-Mediated
1501 Autophagy in Humans. *N Engl J Med* **384**, 2406-2417 (2021).
1502 https://doi.org:10.1056/NEJMoa1915722
1503 70 Evans, R. *et al.* Protein complex prediction with AlphaFold-Multimer. *bioRxiv*,
1504 2021.2010.2004.463034 (2022). https://doi.org:10.1101/2021.10.04.463034
1505 71 Kaiser, S. E. *et al.* Structures of Atg7-Atg3 and Atg7-Atg10 reveal noncanonical
1506 mechanisms of E2 recruitment by the autophagy E1. *Autophagy* **9**, 778-780
1507 (2013). https://doi.org:10.4161/auto.23644
1508 72 Pelaseyed, T. *et al.* Ezrin activation by LOK phosphorylation involves a PIP(2)-
1509 dependent wedge mechanism. *Elife* **6** (2017). https://doi.org:10.7554/eLife.22759

1510 73 Kawaguchi, K. & Asano, S. Pathophysiological Roles of Actin-Binding Scaffold
1511 Protein, Ezrin. *Int J Mol Sci* **23** (2022). https://doi.org:10.3390/ijms23063246
1512 74 Bravo-San Pedro, J. M. *et al.* The LRRK2 G2019S mutant exacerbates basal
1513 autophagy through activation of the MEK/ERK pathway. *Cell Mol Life Sci* **70**,
1514 121-136 (2013). https://doi.org:10.1007/s00018-012-1061-y
1515 75 Alessi, D. R. & Pfeffer, S. R. Leucine-Rich Repeat Kinases. *Annu Rev Biochem*
1516 (2024). https://doi.org:10.1146/annurev-biochem-030122-051144
1517 76 Zhang, Y., Chen, X., Zhao, Y., Ponnusamy, M. & Liu, Y. The role of ubiquitin
1518 proteasomal system and autophagy-lysosome pathway in Alzheimer's disease.
1519 *Rev Neurosci* **28**, 861-868 (2017). https://doi.org:10.1515/revneuro-2017-0013
1520 77 Harris, L. D., Jasem, S. & Licchesi, J. D. F. The Ubiquitin System in Alzheimer's
1521 Disease. *Adv Exp Med Biol* **1233**, 195-221 (2020). https://doi.org:10.1007/978-3-
1522 030-38266-7_8
1523 78 Rotin, D. & Prag, G. Physiological Functions of the Ubiquitin Ligases Nedd4-1
1524 and Nedd4-2. *Physiology (Bethesda)* **39**, 18-29 (2024).
1525 https://doi.org:10.1152/physiol.00023.2023
1526 79 Singh, S. K. *et al.* Astrocytes Assemble Thalamocortical Synapses by Bridging
1527 NRX1alpha and NL1 via Hevin. *Cell* **164**, 183-196 (2016).
1528 https://doi.org:10.1016/j.cell.2015.11.034
1529 80 Kucukdereli, H. *et al.* Control of excitatory CNS synaptogenesis by astrocyte-
1530 secreted proteins Hevin and SPARC. *Proc Natl Acad Sci U S A* **108**, E440-449
1531 (2011). https://doi.org:10.1073/pnas.1104977108

1532 81 Pelaseyed, T. & Bretscher, A. Regulation of actin-based apical structures on
1533 epithelial cells. *J Cell Sci* **131** (2018). https://doi.org:10.1242/jcs.221853
1534 82 Lombardo, A. T., Mitchell, C. A. R., Zaman, R., McDermitt, D. J. & Bretscher, A.
1535 ARHGAP18-Ezrin functions as a RhoA autoregulatory module in the organization
1536 of apical microvilli. *bioRxiv*, 2022.2009.2012.507663 (2022).
1537 https://doi.org:10.1101/2022.09.12.507663
1538 83 Broadhead, M. J. *et al.* Selective vulnerability of tripartite synapses in
1539 amyotrophic lateral sclerosis. *Acta Neuropathol* **143**, 471-486 (2022).
1540 https://doi.org:10.1007/s00401-022-02412-9
1541 84 Blesa, J., Foffani, G., Dehay, B., Bezard, E. & Obeso, J. A. Motor and non-motor
1542 circuit disturbances in early Parkinson disease: which happens first? *Nat Rev*
1543 *Neurosci* **23**, 115-128 (2022). https://doi.org:10.1038/s41583-021-00542-9
1544 85 Hussein, A. *et al.* Non-Motor Symptoms of Parkinson's Disease: The
1545 Neurobiology of Early Psychiatric and Cognitive Dysfunction. *Neuroscientist*,
1546 10738584211011979 (2021). https://doi.org:10.1177/10738584211011979
1547 86 Shenhav, A., Botvinick, M. M. & Cohen, J. D. The expected value of control: an
1548 integrative theory of anterior cingulate cortex function. *Neuron* **79**, 217-240
1549 (2013). https://doi.org:10.1016/j.neuron.2013.07.007
1550 87 Tervo, D. G. R. *et al.* The anterior cingulate cortex directs exploration of
1551 alternative strategies. *Neuron* **109**, 1876-1887 e1876 (2021).
1552 https://doi.org:10.1016/j.neuron.2021.03.028

1553 88 Lanjakornsiripan, D. *et al.* Layer-specific morphological and molecular
1554 differences in neocortical astrocytes and their dependence on neuronal layers.
1555 *Nat Commun* **9**, 1623 (2018). https://doi.org:10.1038/s41467-018-03940-3
1556 89 Bayraktar, O. A. *et al.* Astrocyte layers in the mammalian cerebral cortex
1557 revealed by a single-cell in situ transcriptomic map. *Nat Neurosci* **23**, 500-509
1558 (2020). https://doi.org:10.1038/s41593-020-0602-1
1559 90 Khan, S. S. *et al.* Loss of primary cilia and dopaminergic neuroprotection in
1560 pathogenic LRRK2-driven and idiopathic Parkinson's disease. *bioRxiv*,
1561 2024.2001.2015.575737 (2024). https://doi.org:10.1101/2024.01.15.575737
1562 91 Zimmer, T. S., Orr, A. L. & Orr, A. G. Astrocytes in selective vulnerability to
1563 neurodegenerative disease. *Trends Neurosci* **47**, 289-302 (2024).
1564 https://doi.org:10.1016/j.tins.2024.02.008
1565 92 Murk, K., Blanco Suarez, E. M., Cockbill, L. M., Banks, P. & Hanley, J. G. The
1566 antagonistic modulation of Arp2/3 activity by N-WASP, WAVE2 and PICK1
1567 defines dynamic changes in astrocyte morphology. *J Cell Sci* **126**, 3873-3883
1568 (2013). https://doi.org:10.1242/jcs.125146
1569 93 Savage, J. T. *et al.* SynBot: An open-source image analysis software for
1570 automated quantification of synapses. *bioRxiv* (2024).
1571 https://doi.org:10.1101/2023.06.26.546578
1572 94 Kim, Y. G., Shin, J. J. & Kim, S. J. Minhee Analysis Package: an integrated
1573 software package for detection and management of spontaneous synaptic
1574 events. *Mol Brain* **14**, 138 (2021). https://doi.org:10.1186/s13041-021-00847-x

1575 95 Tan, C. X. *et al.* delta-Catenin controls astrocyte morphogenesis via layer-
1576 specific astrocyte-neuron cadherin interactions. *J Cell Biol* **222** (2023).
1577 https://doi.org:10.1083/jcb.202303138
1578 96 Moffat, J. *et al.* A lentiviral RNAi library for human and mouse genes applied to
1579 an arrayed viral high-content screen. *Cell* **124**, 1283-1298 (2006).
1580 https://doi.org:10.1016/j.cell.2006.01.040
1581 97 Chih, B., Gollan, L. & Scheiffele, P. Alternative splicing controls selective trans-
1582 synaptic interactions of the neuroligin-neurexin complex. *Neuron* **51**, 171-178
1583 (2006). https://doi.org:10.1016/j.neuron.2006.06.005
1584 98 Chen, F. & LoTurco, J. A method for stable transgenesis of radial glia lineage in
1585 rat neocortex by piggyBac mediated transposition. *J Neurosci Methods* **207**, 172-
1586 180 (2012). https://doi.org:10.1016/j.jneumeth.2012.03.016
1587 99 O'Neil, S. D. *et al.* Action potential-coupled Rho GTPase signaling drives
1588 presynaptic plasticity. *Elife* **10** (2021). https://doi.org:10.7554/eLife.63756
1589 100 Ferreira, T. A. *et al.* Neuronal morphometry directly from bitmap images. *Nat*
1590 *Methods* **11**, 982-984 (2014). https://doi.org:10.1038/nmeth.3125
1591 101 Uezu, A. *et al.* Identification of an elaborate complex mediating postsynaptic
1592 inhibition. *Science* **353**, 1123-1129 (2016).
1593 https://doi.org:10.1126/science.aag0821
1594 102 Risher, W. C. *et al.* Thrombospondin receptor alpha2delta-1 promotes
1595 synaptogenesis and spinogenesis via postsynaptic Rac1. *J Cell Biol* **217**, 3747-
1596 3765 (2018). https://doi.org:10.1083/jcb.201802057

1597 103 Kuriata, A. *et al.* CABS-flex 2.0: a web server for fast simulations of flexibility of
1598 protein structures. *Nucleic Acids Res* **46**, W338-W343 (2018).
1599 https://doi.org:10.1093/nar/gky356
1600 104 Takano, T. *et al.* Chemico-genetic discovery of astrocytic control of inhibition in
1601 vivo. *Nature* **588**, 296-302 (2020). https://doi.org:10.1038/s41586-020-2926-0

1602

Figure 1

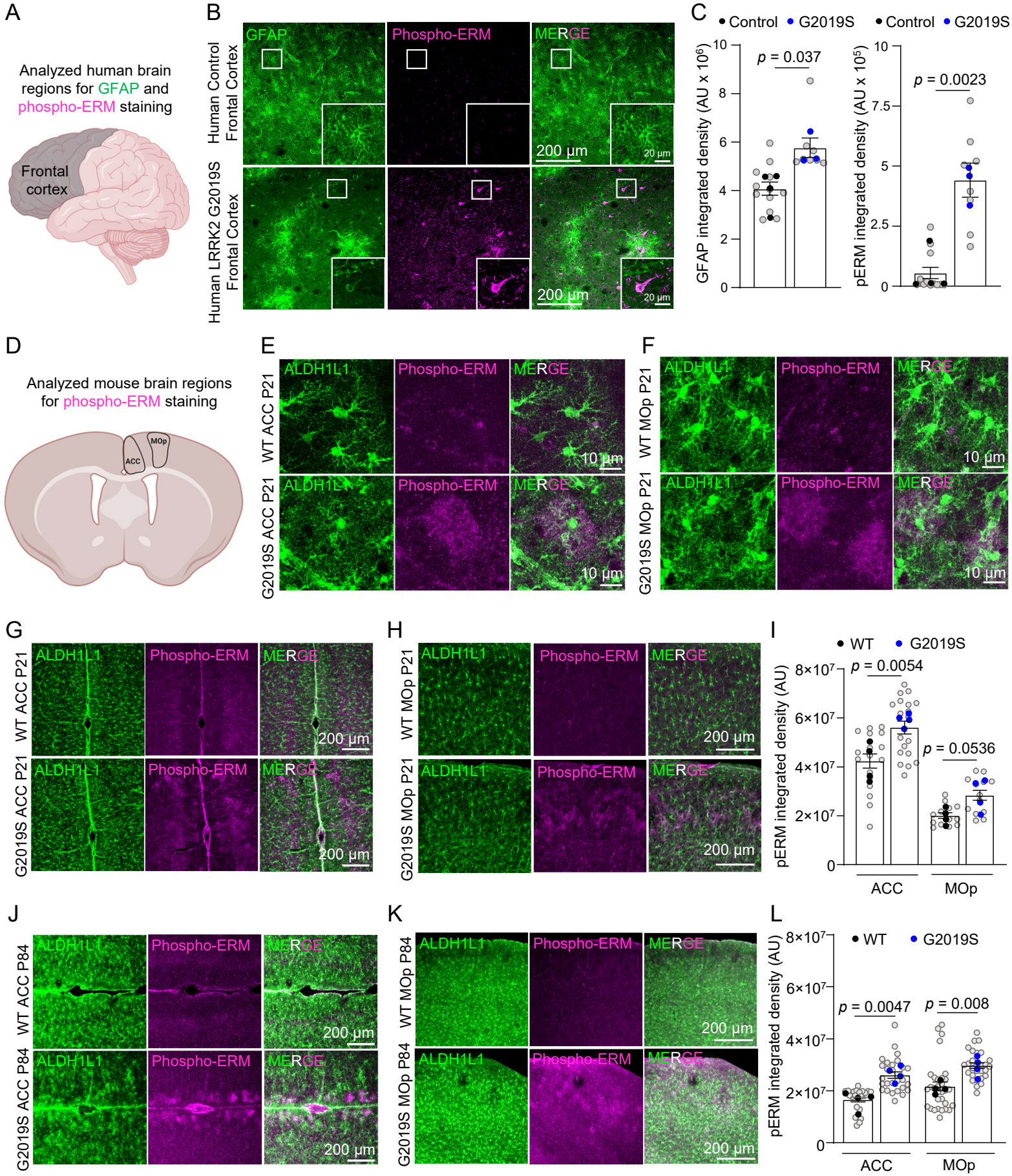
A
Analyzed human brain regions for GFAP and phospho-ERM staining
Frontal cortex
B
Human Control Frontal Cortex
Human LRRK2 G2019S Frontal Cortex
GFAP
Phospho-ERM
MERGE
200 µm
20 µm
C
Control
G2019S
GFAP integrated density (AU x 10^6)
p = 0.037
pERM integrated density (AU x 10^5)
p = 0.0023
D
Analyzed mouse brain regions for phospho-ERM staining
ACC
MOp
E
WT ACC P21
G2019S ACC P21
ALDH1L1
Phospho-ERM
MERGE
10 µm
F
WT MOp P21
G2019S MOp P21
G
WT ACC P21
G2019S ACC P21
H
WT MOp P21
G2019S MOp P21
I
WT
G2019S
pERM integrated density (AU)
p = 0.0054
p = 0.0536
ACC
MOp
J
WT ACC P84
G2019S ACC P84
K
WT MOp P84
G2019S MOp P84
L
p = 0.0047
p = 0.008

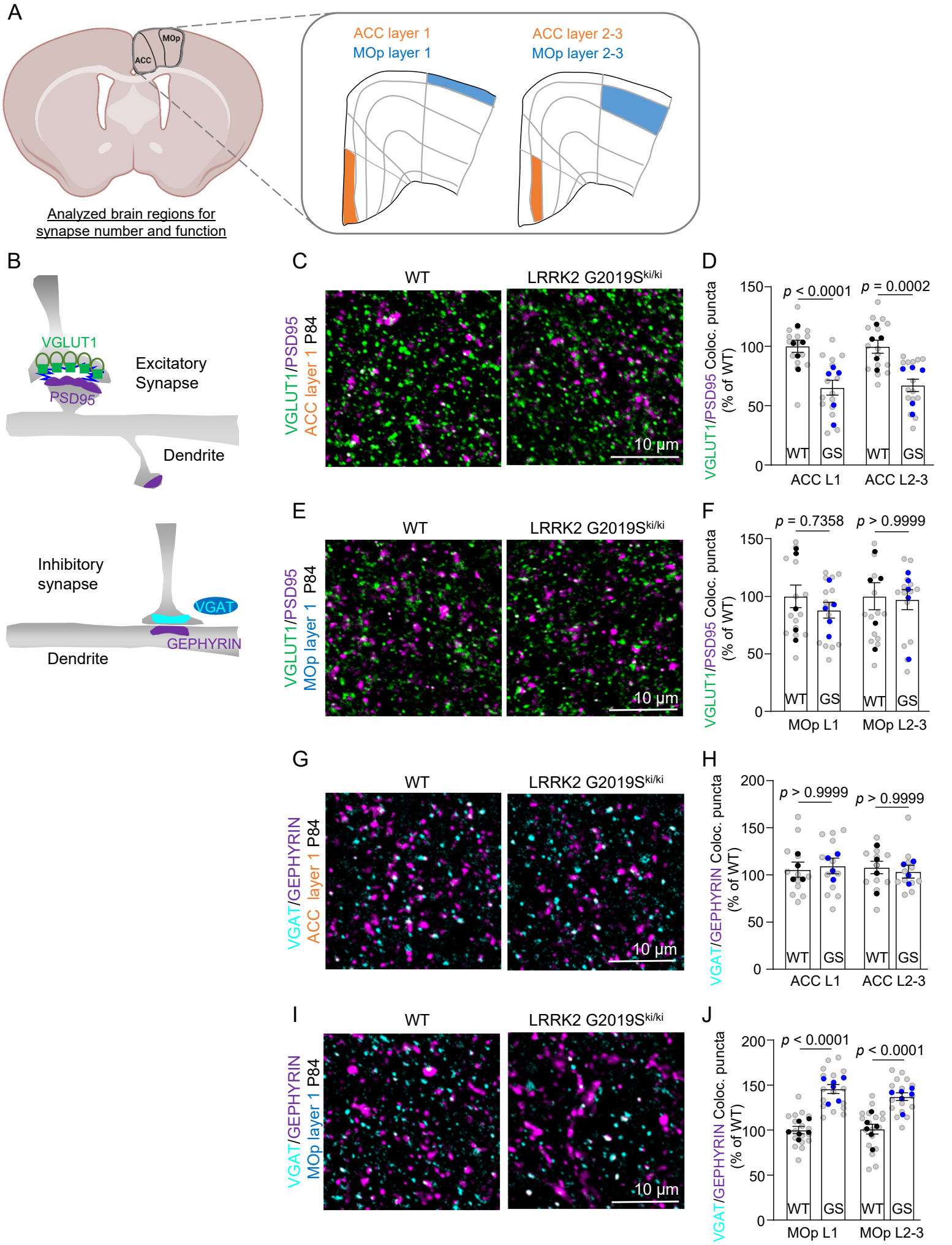
A
MOp
ACC
Analyzed brain regions for synapse number and function
ACC layer 1
MOp layer 1
ACC layer 2-3
MOp layer 2-3
B
VGLUT1
PSD95
Excitatory Synapse
Dendrite
Inhibitory synapse
VGAT
GEPHYRIN
Dendrite
C
WT
LRRK2 G2019S ki/ki
VGLUT1/PSD95
ACC layer 1 P84
10 µm
D
VGLUT1/PSD95 Coloc. puncta (% of WT)
p < 0.0001
p = 0.0002
WT
GS
ACC L1
ACC L2-3
E
VGLUT1/PSD95
MOp layer 1 P84
F
p = 0.7358
p > 0.9999
MOp L1
MOp L2-3
G
VGAT/GEPHYRIN
ACC layer 1 P84
H
VGAT/GEPHYRIN Coloc. puncta (% of WT)
p > 0.9999
I
VGAT/GEPHYRIN
MOp layer 1 P84
J
p < 0.0001

Figure 3

Wang et al.,

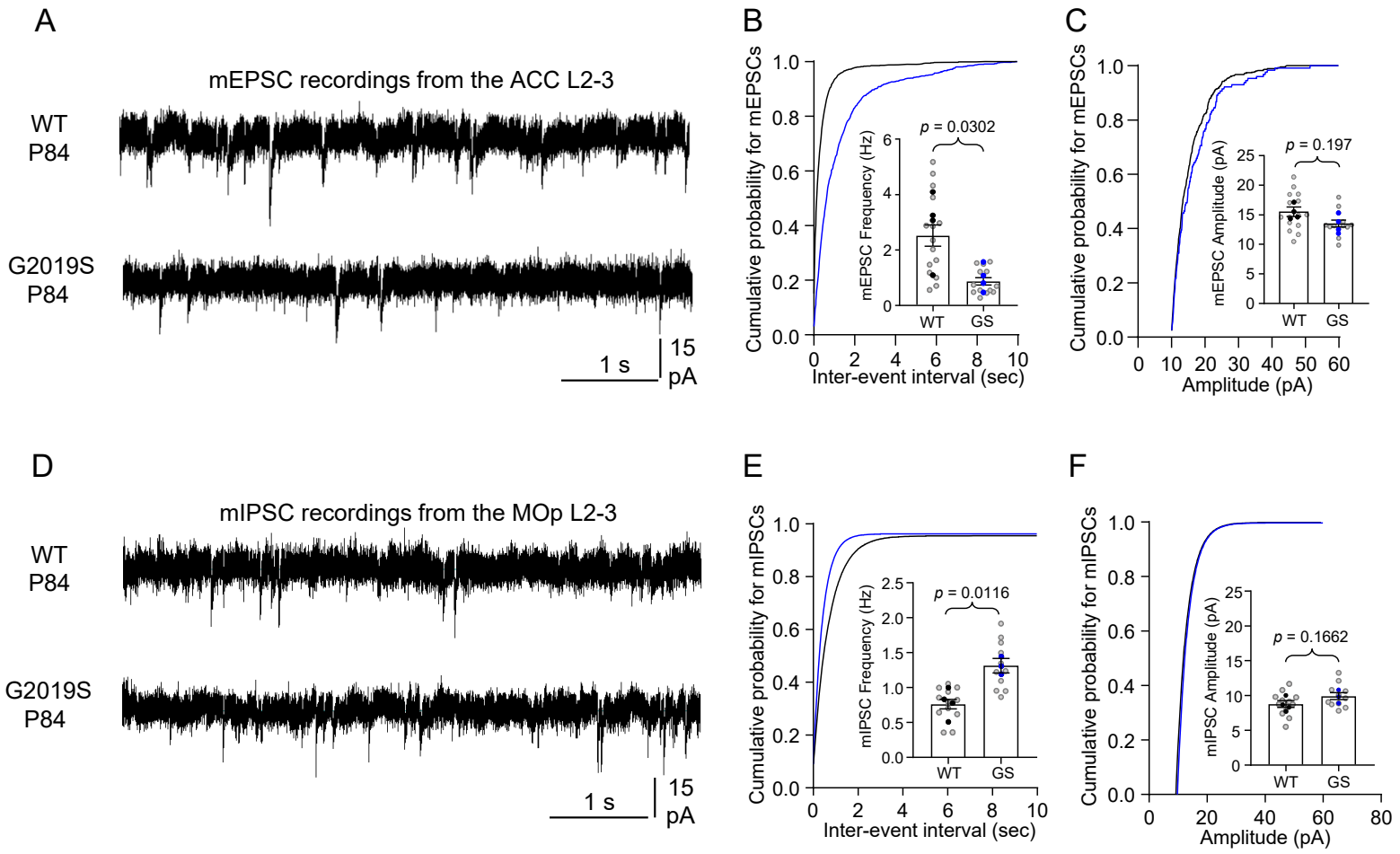

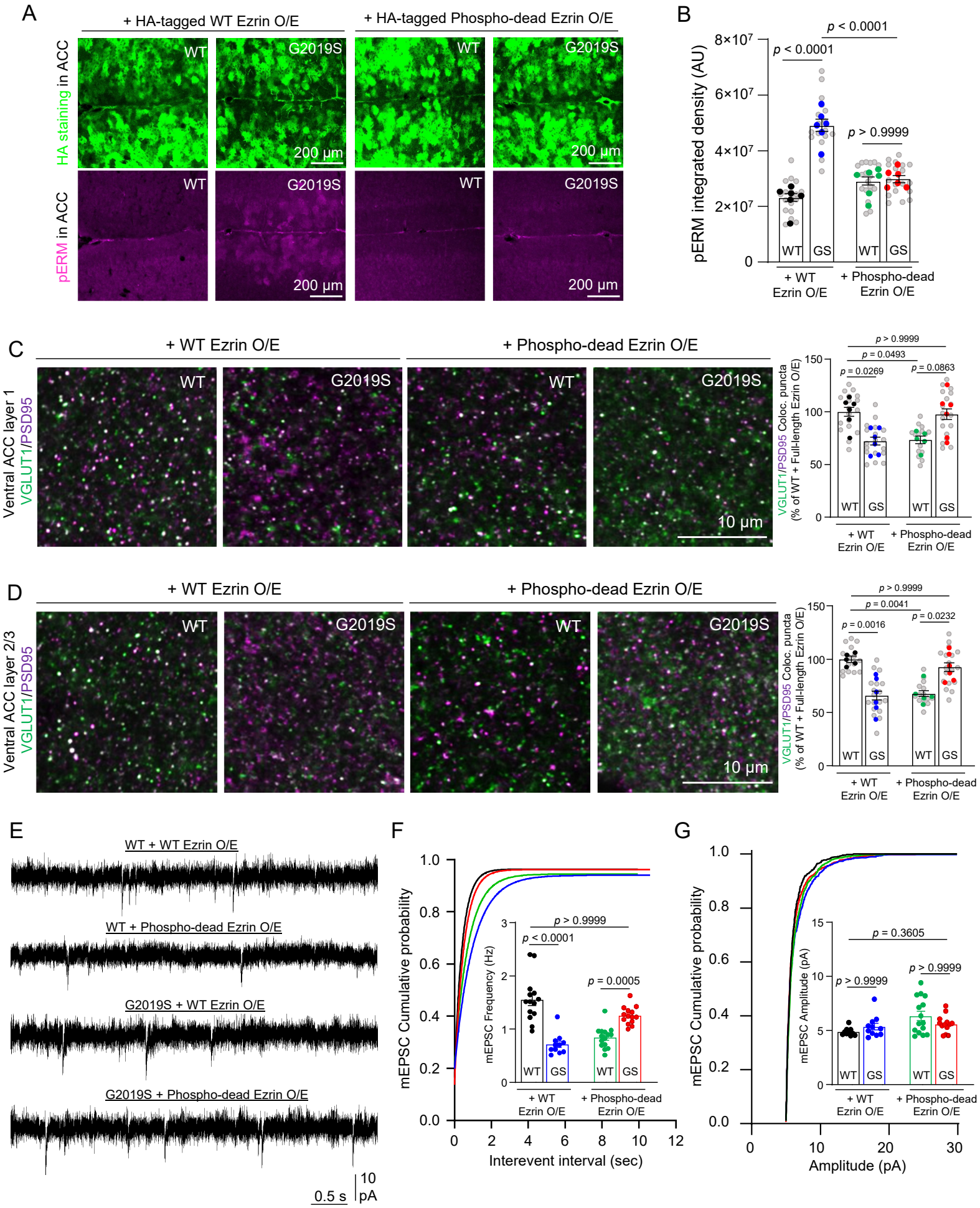
A
+ HA-tagged WT Ezrin O/E
+ HA-tagged Phospho-dead Ezrin O/E
HA staining in ACC
pERM in ACC
WT
G2019S
200 µm
B
pERM integrated density (AU)
p < 0.0001
p > 0.9999
+ WT Ezrin O/E
+ Phospho-dead Ezrin O/E
C
+ WT Ezrin O/E
+ Phospho-dead Ezrin O/E
Ventral ACC layer 1
VGLUT1/PSD95
10 µm
VGLUT1/PSD95 Coloc. puncta (% of WT + Full-length Ezrin O/E)
p = 0.0269
p = 0.0493
p = 0.0863
D
Ventral ACC layer 2/3
p = 0.0016
p = 0.0041
p = 0.0232
E
WT + WT Ezrin O/E
WT + Phospho-dead Ezrin O/E
G2019S + WT Ezrin O/E
G2019S + Phospho-dead Ezrin O/E
0.5 s
10 pA
F
mEPSC Cumulative probability
Interevent interval (sec)
mEPSC Frequency (Hz)
p = 0.0005
G
Amplitude (pA)
mEPSC Amplitude (pA)
p = 0.3605

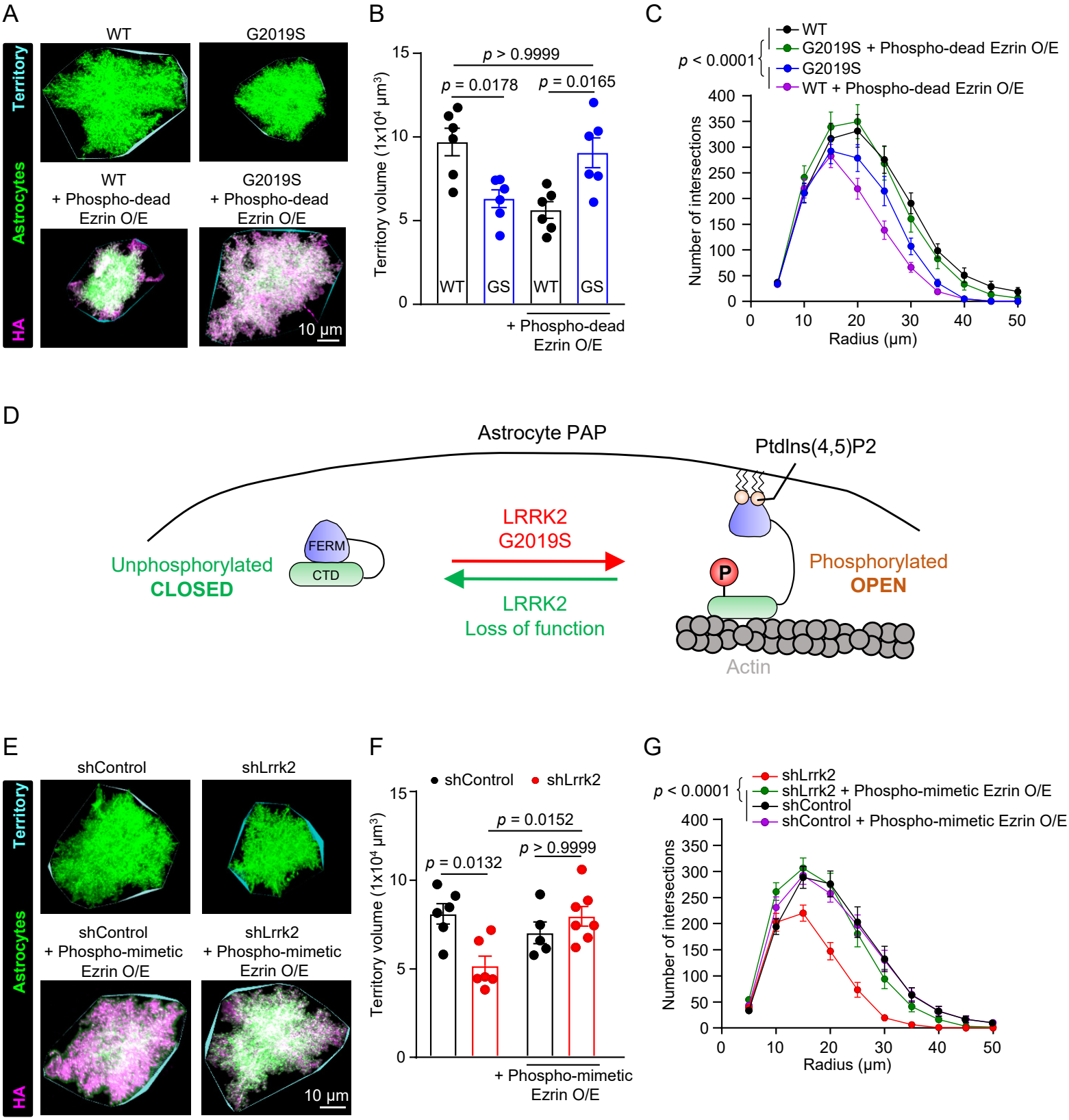
A
WT
G2019S
Territory
Astrocytes
HA
WT + Phospho-dead Ezrin O/E
G2019S + Phospho-dead Ezrin O/E
10 µm
B
Territory volume (1x10⁴ µm³)
p > 0.9999
p = 0.0178
p = 0.0165
WT
GS
WT
GS
+ Phospho-dead Ezrin O/E
C
p < 0.0001
WT
G2019S + Phospho-dead Ezrin O/E
G2019S
WT + Phospho-dead Ezrin O/E
Number of intersections
Radius (µm)
D
Astrocyte PAP
PtdIns(4,5)P2
Unphosphorylated
CLOSED
FERM
CTD
LRRK2
G2019S
LRRK2
Loss of function
P
Phosphorylated
OPEN
Actin
E
shControl
shLrrk2
Territory
Astrocytes
HA
shControl + Phospho-mimetic Ezrin O/E
shLrrk2 + Phospho-mimetic Ezrin O/E
10 µm
F
shControl
shLrrk2
Territory volume (1x10⁴ µm³)
p = 0.0152
p = 0.0132
p > 0.9999
+ Phospho-mimetic Ezrin O/E
G
p < 0.0001
shLrrk2
shLrrk2 + Phospho-mimetic Ezrin O/E
shControl
shControl + Phospho-mimetic Ezrin O/E
Number of intersections
Radius (µm)

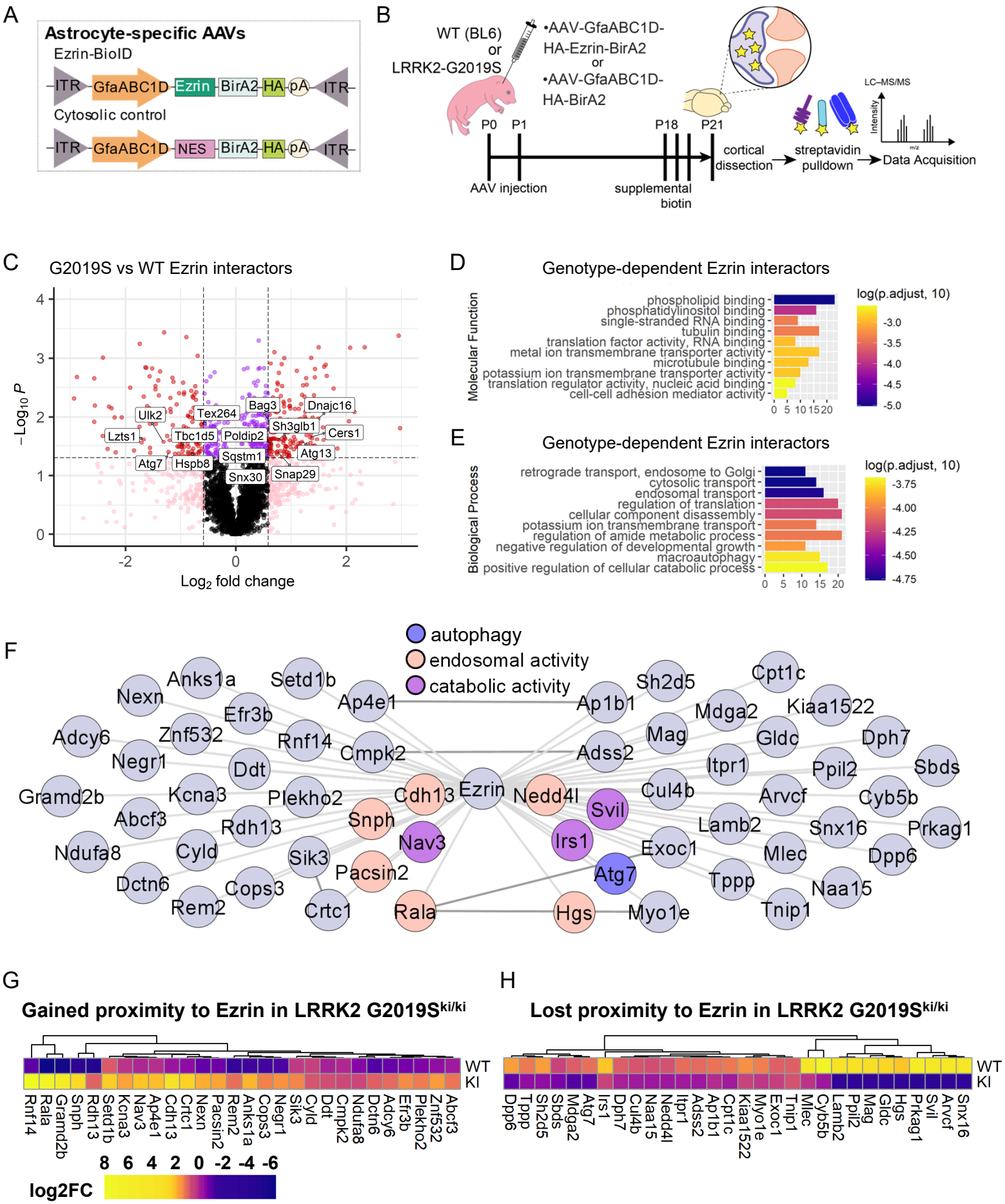
A
Astrocyte-specific AAVs
Ezrin-BioID
ITR GfaABC1D Ezrin BirA2 HA pA ITR
Cytosolic control
ITR GfaABC1D NES BirA2 HA pA ITR
B
WT (BL6) or LRRK2-G2019S
•AAV-GfaABC1D-HA-Ezrin-BirA2 or •AAV-GfaABC1D-HA-BirA2
P0 P1 P18 P21
AAV injection
supplemental biotin
cortical dissection
streptavidin pulldown
LC–MS/MS
Data Acquisition
C
G2019S vs WT Ezrin interactors
−Log10 P
Log2 fold change
Ulk2 Tex264 Bag3 Dnajc16 Lzts1 Tbc1d5 Poldip2 Sh3glb1 Cers1 Atg7 Hspb8 Sqstm1 Atg13 Snx30 Snap29
D
Genotype-dependent Ezrin interactors
Molecular Function
phospholipid binding
phosphatidylinositol binding
single-stranded RNA binding
tubulin binding
translation factor activity, RNA binding
metal ion transmembrane transporter activity
microtubule binding
potassium ion transmembrane transporter activity
translation regulator activity, nucleic acid binding
cell-cell adhesion mediator activity
log(p.adjust, 10)
E
Genotype-dependent Ezrin interactors
Biological Process
retrograde transport, endosome to Golgi
cytosolic transport
endosomal transport
regulation of translation
cellular component disassembly
potassium ion transmembrane transport
regulation of amide metabolic process
negative regulation of developmental growth
macroautophagy
positive regulation of cellular catabolic process
log(p.adjust, 10)
F
autophagy
endosomal activity
catabolic activity
Ezrin
Anks1a Setd1b Nexn Efr3b Ap4e1 Adcy6 Znf532 Rnf14 Negr1 Ddt Cmpk2 Gramd2b Kcna3 Plekho2 Abcf3 Rdh13 Cdh13 Snph Ndufa8 Cyld Nav3 Sik3 Dctn6 Cops3 Pacsin2 Rem2 Crtc1 Rala
Ap1b1 Sh2d5 Cpt1c Mdga2 Kiaa1522 Mag Gldc Dph7 Adss2 Itpr1 Ppil2 Sbds Cul4b Arvcf Cyb5b Nedd4l Svil Lamb2 Snx16 Prkag1 Irs1 Exoc1 Mlec Dpp6 Atg7 Tppp Naa15 Hgs Myo1e Tnip1
G
Gained proximity to Ezrin in LRRK2 G2019Ski/ki
WT
KI
Rnf14 Rala Gramd2b Snph Rdh13 Setd1b Kcna3 Nav3 Ap4e1 Cdh13 Crtc1 Nexn Pacsin2 Rem2 Anks1a Cops3 Negr1 Sik3 Cyld Ddt Cmpk2 Ndufa8 Dctn6 Adcy6 Efr3b Plekho2 Znf532 Abcf3
8 6 4 2 0 -2 -4 -6
log2FC
H
Lost proximity to Ezrin in LRRK2 G2019Ski/ki
WT
KI
Dpp6 Tppp Sh2d5 Sbds Mdga2 Atg7 Irs1 Dph7 Cul4b Naa15 Nedd4l Itpr1 Adss2 Ap1b1 Cpt1c Kiaa1522 Myo1e Exoc1 Tnip1 Mlec Cyb5b Lamb2 Ppil2 Mag Gldc Hgs Prkag1 Svil Arvcf Snx16

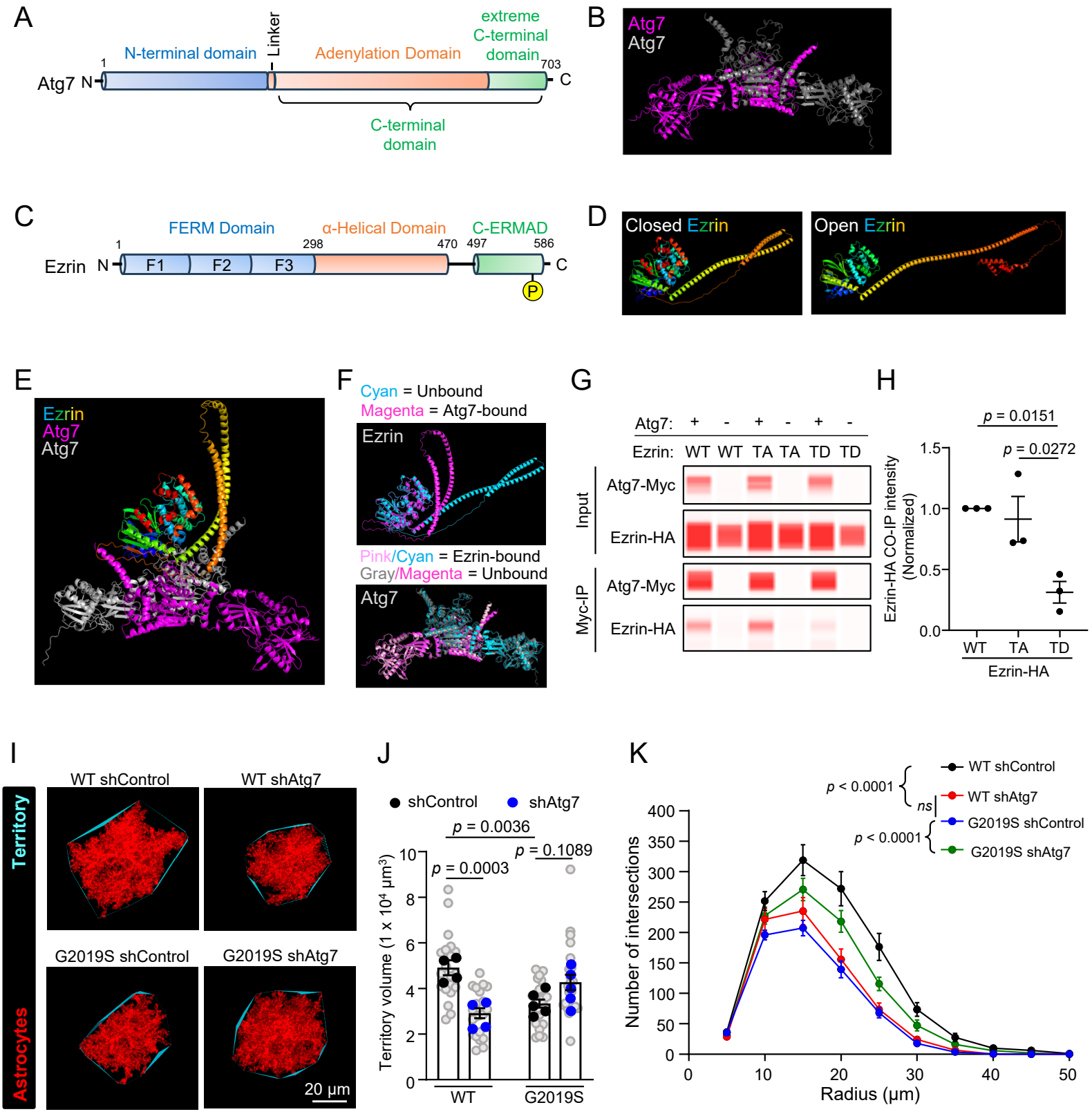
A
Atg7 N
1
N-terminal domain
Linker
Adenylation Domain
extreme C-terminal domain
703
C
C-terminal domain
B
Atg7
Atg7
C
Ezrin N
1
FERM Domain
F1
F2
F3
298
α-Helical Domain
470
497
C-ERMAD
586
C
P
D
Closed Ezrin
Open Ezrin
E
Ezrin
Atg7
Atg7
F
Cyan = Unbound
Magenta = Atg7-bound
Ezrin
Pink/Cyan = Ezrin-bound
Gray/Magenta = Unbound
Atg7
G
Atg7: + - + - + -
Ezrin: WT WT TA TA TD TD
Input
Atg7-Myc
Ezrin-HA
Myc-IP
Atg7-Myc
Ezrin-HA
H
p = 0.0151
p = 0.0272
Ezrin-HA CO-IP intensity (Normalized)
1.5
1.0
0.5
0.0
WT TA TD
Ezrin-HA
I
Territory
Astrocytes
WT shControl
WT shAtg7
G2019S shControl
G2019S shAtg7
20 µm
J
shControl
shAtg7
p = 0.0036
p = 0.0003
p = 0.1089
Territory volume (1 x 10⁴ µm³)
10
8
6
4
2
0
WT
G2019S
K
WT shControl
WT shAtg7
G2019S shControl
G2019S shAtg7
p < 0.0001
ns
p < 0.0001
Number of intersections
400
350
300
250
200
150
100
50
0
0 10 20 30 40 50
Radius (µm)